

TRACKING THE EVOLUTIONARY STAGE OF PROTOSTARS BY THE ABUNDANCES OF ASTROPHYSICAL ICES

W. R. M. ROCHA^{1,2} AND S. PILLING^{3,4}

¹*Instituto de Pesquisa & Desenvolvimento (IP&D), Universidade do Vale do Paraíba, Av. Shishima Hifumi 2911, 12244-000, São José dos Campos, SP, Brazil*

²*Niels Bohr Institute & Centre for Star and Planet Formation, University of Copenhagen, Øster Voldgade 5-7, DK-1350 Copenhagen K., Denmark*

³*Instituto de Pesquisa e Desenvolvimento (IP&D), Universidade do Vale do Paraíba, Av. Shishima Hifumi 2911, 12244-000, São José dos Campos, SP, Brazil*

⁴*Departamento de Física, Instituto Tecnológico de Aeronautica, ITA - DCTA, Vila das Acácias, São José dos Campos, 12228-900, SP-Brazil*

ABSTRACT

The physical evolution of Young Stellar Objects (YSOs) is accompanied by an enrichment of the molecular complexity, mainly triggered by the heating and energetic processing of the astrophysical ices. In this paper, a study of how the ice column density varies across the protostellar evolution has been performed. Tabulated data of H₂O, CO₂, CH₃OH, HCOOH observed by ground- and space-based telescopes toward 27 early-stage YSOs were taken from the literature. The observational data shows that ice column density and spectral index (α), used to classify the evolutionary stage, are well correlated. A 2D continuum radiative transfer simulation containing bare and grains covered by ices at different levels of cosmic-ray processing were used to calculate the Spectral Energy Distributions (SEDs) in different angle inclinations between face-on and edge-on configuration. The H₂O:CO₂ ice mixture was used to address the H₂O and CO₂ column density variation whereas the CH₃OH and HCOOH are a byproduct of the virgin ice after the energetic processing. The simulated spectra were used to calculate the ice column densities of YSOs in an evolutionary sequence. As a result, the models show that the ice column density variation of HCOOH with α can be justified by the envelope dissipation and ice energetic processing. On the other hand, the ice column densities are mostly overestimated in the cases of H₂O, CO₂ and CH₃OH, even though the physical and cosmic-ray processing effects are taken into account.

Keywords: Astrochemistry (75), Infrared sources (793), Interstellar abundances (832), Laboratory astrophysics (2004), Star forming regions (1565)

1. INTRODUCTION

Star formation begins in very embedded regions of Molecular Clouds with no measurable flux in the visible light. Nevertheless, the dust heated by the internal Young Stellar Object (YSOs) emits radiation in infrared (IR) wavelengths. An IR-based classification of protostars have been proposed by Lada & Wilking (1984); Lada (1987); Andre et al. (1993); Greene et al. (1994) and takes into account the IR excess in the Spectral Energy Distributions (SEDs). Formally, the method calculates the spectral index between $2\ \mu\text{m}$ and $24\ \mu\text{m}$ given by:

$$\alpha \equiv \frac{d\log\lambda F_\lambda}{d\log\lambda} \quad (1)$$

where λ is the wavelength and F_λ the flux. The physical structure of each evolutionary stage was reviewed by Williams & Cieza (2011), and the relation with α is also discussed: (i) Class I objects are characterized by a large spherical envelope and a disk, with no optical or near-IR emission and $\alpha_{\text{Class I}} > 0.3$; (ii) Class II are T-Tauri objects with an optically thick disk in the visible, but strong UV emission at short-wavelengths and $-0.3 > \alpha_{\text{Class II}} > -1.6$; (iii) The last stage is defined by Class III objects characterized by a very low infrared excess and $\alpha_{\text{Class III}} < -1.6$. Since Class 0 YSOs are extremely embedded objects, they are not classified by the spectral index. Its classification is, however, given by the ratio between the sub-millimeter luminosity (L_{smm}) and the bolometric luminosity (L_{bol}) as proposed by Andre et al. (1993).

In addition to the physical evolution of YSOs, astrophysical ices play an important role in enriching the chemical complexity in the Interstellar medium. As shown in Boogert et al. (2015), given the conditions of large H/CO gas ratio, $T > 20\ \text{K}$, $n \geq 10^3\ \text{cm}^{-3}$, $A_V > 1.5$, the hydrogenation mechanism leads to the saturation of adsorbed atoms on the dust grain, and the H_2O , CH_4 , NH_3 ices are formed. On the other hand, if H/CO gas ratio is small, $T < 20\ \text{K}$, $n \geq 10^4\ \text{cm}^{-3}$ and $A_V > 3\ \text{mag}$, the CO accretion rate is increased. Thereafter, surface reactions between CO and oxygen atoms might lead to the formation of CO_2 ice. In low-density regions, however, CO_2 ice can be formed via $\text{CO} + \text{OH}$ reactions (Allamandola et al. 1988). In regions denser than $10^4\ \text{cm}^{-3}$, the catastrophic CO freeze-out leads to the efficient formation of methanol ice at low temperatures via carbon monoxide hydrogenation (Watanabe et al. 2003; Fuchs et al. 2009).

Besides the adsorption mechanisms, the chemical enrichment takes place by thermal and energetic processing of the icy compounds. For instance, at around $30\ \text{K}$ the dust grains are warm enough to enable diffusion and

recombination of small molecules on the ice, and complex organic molecules (COMs) are formed (Garrod & Herbst 2006; Herbst & van Dishoeck 2009; Caselli & Ceccarelli 2012). On the other hand, the energetic processing of ices is the main route to form complex species as reviewed by Öberg (2016) for photochemical induced processes and particles by Boduch et al. (2015); Rothard et al. (2017).

In order to investigate how the abundance of ice species are related to the evolutionary sequence, tabulated data of ice column density and spectral index of 27 YSOs were taken from Pontoppidan et al. (2008); Boogert et al. (2008). Additionally, 2D continuum radiative transfer models of protostars in an evolutionary sequence, containing dust grains covered by ice at different levels of processing was used to simulate how the ice column density varies with the protostar evolution.

The paper is structured as follows: Section 2 shows the source sample addressed in this paper, and Section 3 shows the ice column density decreasing with the spectral index i.e. as the protostar evolves. Section 4 characterizes the radiative transfer simulations and the ice-dust model and shows how the laboratory data were employed in the simulations. In Section 5 the results and discussion are shown, and the conclusions are in Section 6. Appendix A detail how the IR range between $5.5\text{--}7.5\ \mu\text{m}$ was decomposed using Gaussian profiles.

2. SOURCE SAMPLE

Table 1 lists 27 well-known Low-Mass Young Stellar Objects (LYSOs) addressed in this paper. Both the evolutionary stage and the column densities for these sources were directly taken from Boogert et al. (2008) and Pontoppidan et al. (2008). The authors used broadband ($2.17\text{--}24\ \mu\text{m}$) classification scheme to calculate the spectral index through Equation 1, and cover Class 0/I to Class I/II. The spectral index error bar was not provided.

Spitzer data in the mid-IR, combined with ground-based observations in the near-IR (Keck NIRSPEC (McLean et al. 1998) and VLT-ISAAC (Moorwood 1997)), when available, were used to calculate the ice column densities the sources listed in Table 1. The IR spectrum was converted into optical depth using the equation $\tau_\lambda = -\ln\left(\frac{F_\lambda^{\text{obs}}}{F_\lambda^{\text{cont}}}\right)$ to allow the column density calculation, where F_λ^{obs} is the observed flux and F_λ^{cont} is the SED continuum. The continuum was defined by a low-order polynomial for all the sources. Thereafter, the ice column density was calculated by:

$$N_{\text{ice}} = \frac{1}{\mathcal{A}} \int_{\nu_1}^{\nu_2} \tau_\nu d\nu \quad (2)$$

where \mathcal{A} is the band strength of a specific vibrational mode and ν is the wavenumber in units of cm^{-1} .

In Boogert et al. (2008), the H_2O ice column density was calculated from the O–H stretching mode at $3.0 \mu\text{m}$, or the libration mode at $12.3 \mu\text{m}$, after the removal of the contribution of silicate absorption. The bending mode at $6.0 \mu\text{m}$ has been avoided, since such a band cannot be attributed only to water as reported in Gibb et al. (2000); Keane et al. (2001); Gibb et al. (2004). Methanol ice column density was derived from

the absorption features at $3.54 \mu\text{m}$ and $9.7 \mu\text{m}$. Formic acid (HCOOH), has many vibrational modes in the IR, but its column density was calculated from the band at $7.25 \mu\text{m}$, since the other modes are blended with H_2O and other alcohols such as ethanol and methanol. The carbon dioxide ice column density in Pontoppidan et al. (2008), was calculated from the bending mode at $15.2 \mu\text{m}$. Table 2 shows the column densities calculated for the ices mentioned above.

Table 1. Source sample

Source	R.A. (J2000)	DEC (J2000)	Cloud	α_{IR}	Stage	Telescope
IRAS 03245+3002	03h27'39.03"	+30°12'59.3"	Perseus	2.70	Class 0/I	Spitzer
L1455 SMM 1.....	03h27'43.25"	+30°12'28.8"	Perseus	2.41	Class 0/I	Spitzer
IRAS 03271+3013	03h30'15.16"	+30°23'48.8"	Perseus	2.06	Class 0/I	Spitzer, Keck
B1-c.....	03h33'17.89"	+31°09'31.0"	Perseus	2.66	Class 0/I	Spitzer
HH 46 IRS.....	08h25'43.78"	-51°00'35.6"	HH 46	1.70	Class 0/I	Spitzer, VLT
CRBR 2422.8-3423.....	16h27'24.61"	-24°41'03.3"	Oph	1.60	Class 0/I	Spitzer, Keck
SSTe2d J171122.2-272602 .	17h11'22.16"	-27°26'02.3"	B59	2.26	Class 0/I	Spitzer
2MASS J17112317-2724315	17h11'23.13"	-27°24'32.6"	B59	2.48	Class 0/I	Spitzer, Keck
CrA IRS 7A	19h01'55.32"	-36°57'22.0"	CrA	2.23	Class 0/I	Spitzer, VLT
CrA IRAS 32.....	19h02'58.69"	-37°07'34.5"	CrA	2.15	Class 0/I	Spitzer
L1014 IRS.....	21h24'07.51"	+49°59'09.9"	L1014	1.60	Class 0/I	Spitzer, Keck
L1489 IRS.....	04h04'43.07"	+26°18'56.4"	Taurus	1.10	Class I	Spitzer, Keck
HH 300.....	04h26'56.30"	+24°43'35.3"	Taurus	0.79	Class I	Spitzer, Keck
DG Tau B.....	04h27'02.66"	+26°05'30.5"	Taurus	1.16	Class I	Spitzer, Keck
IRAS 12553-7651	12h59'06.63"	-77°07'40.0"	Cha	0.76	Class I	Spitzer
Elias 29.....	16h27'09.42"	-24°37'21.1"	Oph	0.53	Class I	ISO
IRAS 17081-2721	17h11'17.28"	-27°25'08.2"	B59	0.55	Class I	Spitzer, Keck
EC 82	18h29'56.89"	+01°14'46.5"	Serpens	0.38	Class I	Spitzer
SVS 4-5.....	18h29'57.59"	+01°13'00.6"	Serpens	1.26	Class I	Spitzer, VLT
R CrA IRS 5.....	19h01'48.03"	-36°57'21.6"	CrA	0.98	Class I	Spitzer, VLT
HH 100 IRS.....	19h01'50.56"	-36°58'08.9"	CrA	0.80	Class I	ISO
RNO 15.....	03h27'47.68"	+30°12'04.3"	Perseus	-0.21	Class I/II	Spitzer, Keck
IRAS 13546-3941	13h57'38.94"	-39°56'00.2"	BHR 92	-0.06	Class I/II	Spitzer
RNO 91.....	16h34'29.32"	-15°47'01.4"	L43	0.03	Class I/II	Spitzer, VLT
EC 74	18h29'55.72"	+01°14'31.6"	Serpens	-0.25	Class I/II	Spitzer, Keck
EC 90	18h29'57.75"	+01°14'05.9"	Serpens	-0.09	Class I/II	Spitzer
CK 4	18h29'58.21"	+01°15'21.7"	Serpens	-0.25	Class I/II	Spitzer

Table 2. Ice column density of the Source sample.

Source	$N_{\text{H}_2\text{O}}^a$ (10^{18} cm^{-2})	$N_{\text{CO}_2}^c$ (10^{18} cm^{-2})	$N_{\text{CH}_3\text{OH}}^a$ (10^{18} cm^{-2})	$N_{\text{HCOOH}}^{a,e}$ (10^{18} cm^{-2})
IRAS 03245+3002	39.31 ± 5.65^b	-	3.85	0.47
L1455 SMM 1	18.21 ± 2.82^b	6.34 ± 0.44	2.45	0.60 ± 0.02
IRAS 03271+3013	7.69 ± 1.76^b	1.53 ± 0.09	0.43	0.19
B1-c	29.55 ± 5.65^b	8.4	2.1	0.35 ± 0.01
HH 46 IRS	7.79 ± 0.77	2.16 ± 0.01	0.42 ± 0.01^d	0.21 ± 0.01
CRBR 2422.8-3423	4.19 ± 0.41	1.05 ± 0.01	0.38	-
SSTc2d J171122.2-272602	13.94 ± 2.92^b	-	0.18	0.41 ± 0.03
2MASS J17112317-2724315	19.49 ± 0.23^b	-	0.62	0.48 ± 0.16
CrA IRS 7A	10.89 ± 1.92^b	1.96 ± 0.12	0.41	-
CrA IRAS 32	5.26 ± 1.88^b	1.87 ± 0.21	0.95	-
L1014 IRS	7.16 ± 0.91^b	-	0.22 ± 0.05	-
L1489 IRS	4.26 ± 0.51	1.62 ± 0.02	0.21 ± 0.01	0.12
HH 300	2.59 ± 0.25	-	0.17	0.06
DG Tau B	2.29 ± 0.39	0.54	0.13	0.07
IRAS 12553-7651	2.98 ± 0.56^b	0.61 ± 0.01	0.08	0.05
Elias 29	3.04 ± 0.30	0.84 ± 0.06	0.14^d	0.04
IRAS 17081-2721	1.31 ± 0.13	-	0.04^d	0.03
EC 82	0.39 ± 0.07	0.25 ± 0.01	0.05	0.01
SVS 4-5	5.65 ± 1.13	1.72 ± 0.05	1.41 ± 0.19^d	-
R CrA IRS 5	3.58 ± 0.26	1.42 ± 0.02	0.23 ± 0.04	0.15
HH 100 IRS	2.45 ± 0.24	-	0.23^d	0.06
RNO 15	0.69 ± 0.06	0.25 ± 0.01	0.03^d	0.04
IRAS 13546-3941	2.07 ± 0.21^b	0.87 ± 0.02	0.08	-
RNO 91	4.25 ± 0.36	1.16 ± 0.02	0.24	-
EC 74	1.07 ± 0.18	0.30 ± 0.05	0.1^d	0.03
EC 90	1.69 ± 0.16	0.54 ± 0.05	0.11 ± 0.01	0.06
CK 4	1.50 ± 0.01	0.20 ± 0.01	-	-

NOTE—^a Taken from [Boogert et al. \(2008\)](#).

^b $N_{\text{H}_2\text{O}}$ calculated from the H_2O libration mode at $13.6 \mu\text{m}$ using the band strength $\mathcal{A}_{\text{H}_2\text{O}} = 2.8 \times 10^{-17} \text{ cm molecule}^{-1}$. The stretching mode at $3 \mu\text{m}$ was used in the other cases.

^c Taken from [Pontoppidan et al. \(2008\)](#).

^d The column densities was calculated from the absorption features at $3.53 \mu\text{m}$, using the band strength of $\mathcal{A}_{\text{CH}_3\text{OH}} = 5.6 \times 10^{-18} \text{ cm molecule}^{-1}$. The absorption at $9.7 \mu\text{m}$ was used in the other cases, assuming the band strength of $\mathcal{A}_{\text{CH}_3\text{OH}} = 1.6 \times 10^{-17} \text{ cm molecule}^{-1}$.

^e The column densities was calculated from the absorption features at $7.25 \mu\text{m}$, using the band strength of $\mathcal{A}_{\text{HCOOH}} = 1.5 \times 10^{-17} \text{ cm molecule}^{-1}$.

3. CORRELATIONS BETWEEN ICE COLUMN DENSITY AND SPECTRAL INDEX

Figure 1 shows the ice column density and the spectral index (α) for the Class 0/I, Class I and Class I/II, given by the black squares, red circles and blue triangles, re-

spectively. H₂O is the most abundant ice toward all the sources, followed by CO₂, CH₃OH and HCOOH, which agrees with the expected abundances shown by Öberg et al. (2011).

Very early stages of the protostellar evolution are dominated by a cold envelope under gravitational collapse. Jørgensen et al. (2009) found evidence of envelope dissipation, estimated from the increasing of the disk-envelope mass ratio in ten Class 0 and Class I systems. Such a trend has also been observed in Andersen et al. (2019) toward the Perseus Molecular Cloud, where they also found strong evidence of the disk growth at Class 0 stage.

Since the ices are formed onto dust grains in cold regions, the dusty envelope dissipation might lead to an ice column density decreasing, as suggested in Figure 1. In order to make easier the comparison between N_{ice} and α in this paper, an exponential function given by the Equation 3 has been assumed:

$$N_{\text{ice}} = N_{\text{ice}}^{\text{plateau}} + s \cdot e^{r \cdot \alpha} \quad (3)$$

where $N_{\text{ice}}^{\text{plateau}}$ is the ice column density *plateau* toward the line of sight, s is a scale factor of the amplitude variation in the y-axis and r the decreasing rate (positive since x-axis is inverted). Since the presence of foreground clouds toward star-forming regions has been reported in the literature (Boogert et al. 2002b; Pontoppidan et al. 2005; van Dishoeck et al. 2011; Smith et al. 2015), the term $N_{\text{ice}}^{\text{plateau}}$ aims to take into account this factor. To compare the goodness of the fit among the ice species, the reduced χ^2 was used, given by $\chi_{\nu}^2 = \chi^2 / (n - m)$, where n is the number of data points, and m is the degree of freedom. Acceptable fits requires $\chi_{\nu}^2 \sim 1$.

Table 3 shows the parameters obtained from the exponential fit as well as the χ_{ν}^2 . The $N_{\text{H}_2\text{O}}^{\text{plateau}}$ and $N_{\text{CO}_2}^{\text{plateau}}$ are in agreement with the ice column densities in foreground clouds proposed in the literature. In fact, Boogert et al. (2000) suggest that only 30% of the ice column density observed toward Elias 29 protostar belong to the object itself, whereas a *plateau* of around $N_{\text{H}_2\text{O}} \sim 2 \times 10^{18} \text{ cm}^{-2}$ is hosted by foreground clouds. Toward CRBR 2422.8–3423, Pontoppidan et al. (2005) estimate that, at least, 50% of the H₂O ice column density lies in foreground clouds, namely, $N_{\text{H}_2\text{O}} \leq 1.8 \times 10^{18} \text{ cm}^{-2}$. For face-on Class II YSO 2MASSJ 1628137 in Taurus, the estimated ice column density is about one order of magnitude lower than for the previous Class I objects, i.e. $N_{\text{H}_2\text{O}} \sim 0.2 \times 10^{18} \text{ cm}^{-2}$ (Aikawa et al. 2012). In the case of CO₂ ice, the estimated column density in foreground clouds are $N_{\text{CO}_2} \sim 2 \times 10^{17} \text{ cm}^{-2}$ in Elias 29 (Boogert et al. 2000) and $N_{\text{CO}_2} \leq 6 \times 10^{17}$

cm^{-2} (Pontoppidan et al. 2005) in CRBR 2422.8–3423. In the case of CH₃OH and HCOOH, the derived parameters must be used with caution due to the poor fit indicated by the χ_{ν}^2 .

From the decreasing rate (r), one can observe that CO₂ ice decreases slower than H₂O with the protostellar evolution. Due to the lower thermal desorption of pure CO₂ ($\sim 75 \text{ K}$), the most probable scenario in the Interstellar Medium is that C-rich molecules are trapped in a H₂O ice matrix. In this case, part of the CO₂ ice is only released back to the gas-phase at around 150 K, that characterizes the H₂O temperature desorption (Collings et al. 2004). In addition, the CO₂ ice can be formed via a surface reaction between OH and CO as shown by Allamandola et al. (1988). As a consequence, in an environment dominated by radiation, CO₂ is slowly destroyed compared to H₂O because of its reformation mechanism from the water photo-products. Regarding formic acid and methanol, although the fits indicate that their respective ice column densities drop slower and faster with the spectral index, this result can be called into question due to the poor exponential fit. If, however, this is a real effect, a likely explanation is the efficient HCOOH formation both in gas- and solid-phase compared to CH₃OH Agúndez & Wakelam (2013). To allow easier comparison between all the fits, Figure 1f shows the normalized ice column densities for the four ices addressed in this paper.

In order to address if the envelope dissipation, viewing angle and the energetic processing of ices are able to provide a likely explanation for the ice column density variation shown in Figure 1, a computational model of YSOs at different stages surrounded by dust and ice was employed in this paper. To mimic the energetic processing of the ices across the protostellar evolution, laboratory data of H₂O:CO₂ taken from Pilling et al. (2010) and Rocha et al. (2017) has also been used.

4. MODELS OF YSOS SURROUNDED BY DUST AND ICE

Whitney et al. (2003) describes the physical evolution of YSOs in an evolutionary sequence, by using the 2D radiative transfer code HO-CHUNK¹. In this paper, however, the models used by Whitney et al. are employed as a template, and laboratory data of energetically processed ice are included in the simulations to address how the ice column density changes during the protostellar evolution. The physical parameters adopted in these simulations and the dust-ice model are, described in the next sections.

¹ <http://gemelli.colorado.edu/~bwhitney/codes/codes.html>

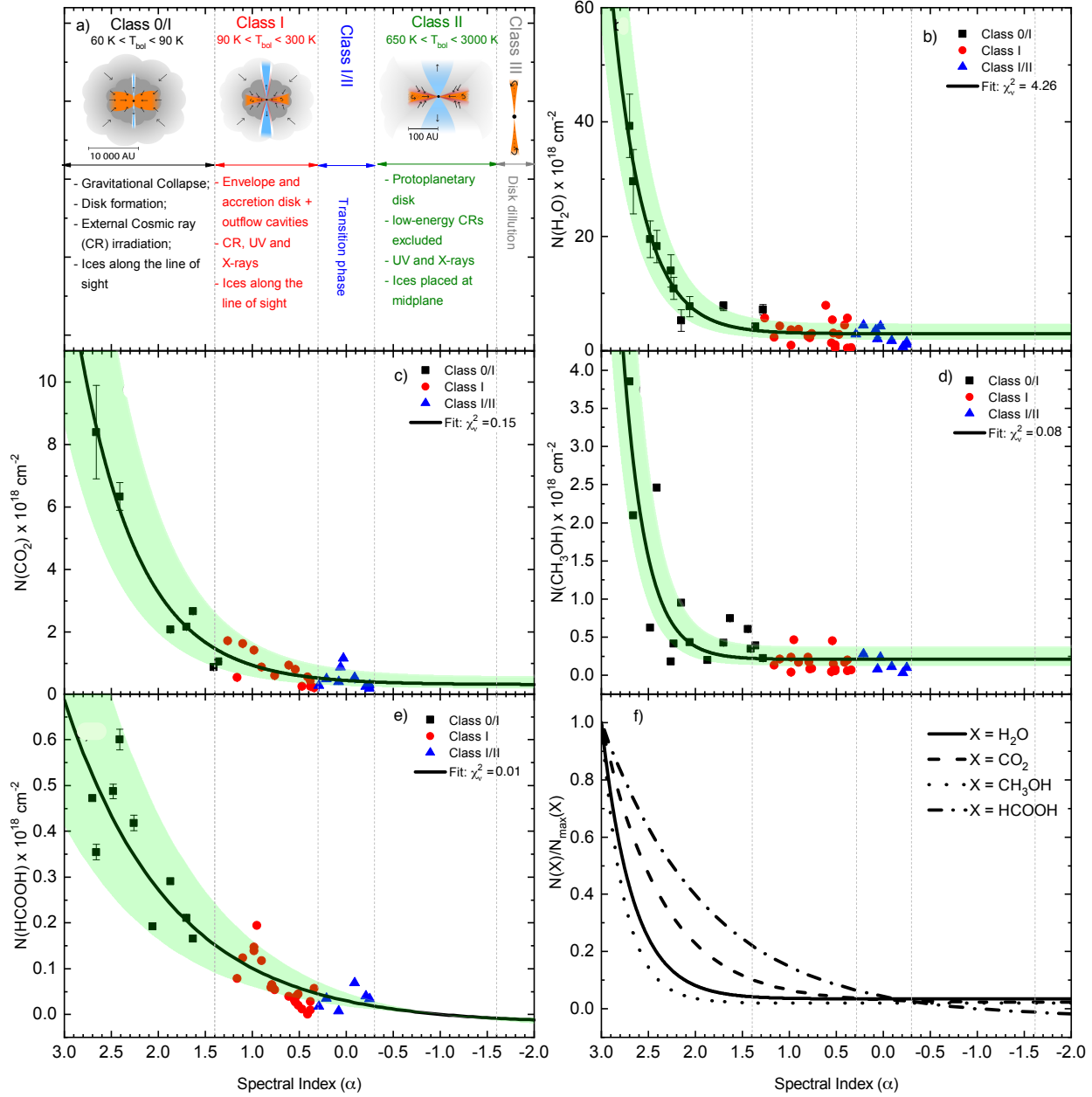


Figure 1. Column density correlation of the frozen molecules H_2O , CO_2 , CH_3OH , HCOOH with the spectral index (α). Panel a shows a schematic representation of the structure of YSO for each evolutionary stage (Persson 2014). The colours and symbols in panels (b - e) represent the evolutionary stages of protostars and the green shaded area corresponds to 99% confidence interval. The exponential fit is shown by the solid black line. Panel f compares all fits for the normalized data.

Table 3. Parameters obtained from the exponential fit in Figure 1

Ice specie	$N_{\text{ice}}^{\text{plateau}} \times 10^{18} [\text{cm}^2]$	Scale factor (s) $\times 10^{17} [\text{cm}^2]$	Decreasing rate (r)	χ^2_{ν}
H ₂ O	2.9 ± 0.4	9.7 ± 2.7	3.0 ± 0.2	4.26
CO ₂	0.3 ± 0.1	1.3 ± 0.4	1.5 ± 0.1	0.15
CH ₃ OH ^a	0.2	4.6	4.2	0.08
HCOOH ^a	-0.03	0.1	0.64	0.01

^a Due to the poor fitting with the exponential function, the error bars of the derived parameters are now shown.

4.1. Template models

All models share the same parameters of the central star, namely, $R(R_\odot) = 2.09$, $T(K) = 4000$ K, $M(M_\odot) = 0.5$ and $L(L_\odot) = 1.0$. A flared disk in hydrostatic equilibrium is set by the density profile below:

$$\rho_{disk} = \rho_0 \left(1 - \sqrt{\frac{R_\star}{\bar{\omega}}} \right) \left(\frac{R_\star}{\bar{\omega}} \right)^\alpha \exp \left\{ -\frac{1}{2} \left[\frac{z}{h(\bar{\omega})} \right]^2 \right\}, \quad (4)$$

where $\bar{\omega}$ is the radial coordinate in the disk midplane, and $h = h_0 (\bar{\omega}/R_\star)^\beta$ is the scale height. It assumed in all models that $\alpha = 2.25$, $\beta = 1.25$ and a inner disk scale height $h_0 = 0.01$. The infalling envelope is characterized by the Ulrich's density structure (Ulrich 1976), given by:

$$\rho_{env} = \frac{\dot{M}_{env}}{4\pi} \left(\frac{GM_\star}{R_c^3} \right)^{-1/2} \left(\frac{r}{R_c} \right)^{-3/2} \left(1 - \frac{\mu}{\mu_0} \right)^{-1/2} \left(\frac{\mu}{\mu_0} + \frac{2\mu_0^2 R_c}{r} \right)^{-1}, \quad (5)$$

where \dot{M}_{env} is the envelope mass infall rate, R_c the centrifugal radius and $\mu = \cos(\theta)$. θ is the angle from the axis of symmetry and μ_0 is the cosine polar angle of a streamline of infalling particles for $r \rightarrow \infty$ given by

$$\mu_0^3 + \mu_0 \left(\frac{r}{R_c} - 1 \right) - \mu \left(\frac{r}{R_c} \right) = 0. \quad (6)$$

The evolutionary sequence is simulated by varying the parameters in Equations 4 - 6 for the disk and envelope, as shown in Table 4. The values used for each evolutionary stage were constrained from previous observational and theoretical works as pointed out by Whitney et al. (2003). Briefly, these models start with the central protostar surrounded by a massive envelope with a high infall rate, that decreases across the evolution. The disk mass remains constant from Class 0/I to Class II, and decreases in 6 orders of magnitude in Class III. Both inner and outer disk and envelope radius are the same as Whitney et al. (2003). As expected from on images of molecular outflows, the cavity angle increases with the age, whereas the cavity density decreases (Padgett et al. 1999; Mottram et al. 2017; de Valon et al. 2020).

4.2. Dust and ice properties

The dust properties in the models changes between the envelope, outflow cavity, upper disk layers and midplane regions. Since that physical processes such as settling and coagulation (Henning & Semenov 2013) might take place at the midplane, millimeter-sized grains (~ 1 mm) where placed in dense regions given by $n_{H_2} > 10^8$ cm $^{-3}$.

The upper disk layers ($n_{H_2} < 10^8$ cm $^{-3}$) were populated by grains with size between 1-10 μ m. For the envelope, a size distribution between 0.5-1.0 μ m was adopted, whereas a fixed size of 0.1 μ m was used for the cavity region. It should be mentioned that all these dust models are already available in the HO-CHUNCK code.

The ice mantle is the new part in these models, compared to the original paper. Although the authors have also used H₂O ice in their models, this paper employs an ice composition given by the mixture of H₂O:CO₂ (1:1) processed by $^{58}\text{Ni}^{13+}$ ions from its pristine composition: (i) Fluence 0 (Virgin ices), (ii) Fluence 1×10^{12} ions cm $^{-2}$ (first processing) and (iii) Fluence 1×10^{13} ions cm $^{-2}$ (second processing) obtained from Pilling et al. (2010) (see Figure 2a). As calculated by Drury et al. (2000) and Shen et al. (2004), the ^{58}Ni flux is around 6.4×10^{-6} cm $^{-2}$ s $^{-1}$, which corresponds to a relative time to the virgin ice of 5×10^5 year and 5×10^6 year for the Fluences 1 and 2, respectively. These two irradiated ice spectra were selected from the whole range of experiments because they cover the timescales of Class I and Class II YSOs. The inner panels in Figure 2a show the ice features that will be used to calculate the ice column densities, except the range between 14–17 μ m. It is important to note from the shape of the O-H stretching mode that no water crystallization is induced by the CR processing, although the ice segregation is evident from the formation of the double peak of CO₂ feature at 15 μ m.

Although the CO₂/H₂O ratio is expected to be around 30% toward low-mass YSOs (Öberg et al. 2011), a higher ratio is used in this paper. Even though this high CO₂ fraction is unlikely for the star-forming regions, it was used in the experiments to maximize the formation of C-bearing products. However, as a product of the ice processing in the experiments, carbon monoxide ice was only detectable in the laboratory spectrum after the first irradiation dose, thereby being destroyed at high fluences. Given this unique detection of CO ice in the selected experiments used in this paper, its chemical evolution with the evolutionary stage of YSOs was not addressed in this paper. Another sample containing CO in the initial mixture could be also explored. The effective interaction limit of other ionizing agents as UV and X-rays is much lower compared to Cosmic Rays (Indriolo & McCall 2013) in dense regions such as the protostellar envelope. Cosmic ray-processing, on the other hand, might remove electrons from the inner shells of atoms, or excite H₂ molecules, leading to an induced X-ray and/or UV radiation field.

The optical constants of the H₂O:CO₂ ices were taken from Rocha et al. (2017) (Figure 2b-c). In order to

Table 4. Physical parameters used in the 2D continuum radiative transfer simulation.

Parameter	Class 0/I	Class I	Class I/II	Class II	Class III
Envelope infall rate (\dot{M}_{env}) [$M_{\odot} yr^{-1}$]	1×10^{-5}	5×10^{-6}	1×10^{-6}	0	0
Envelope mass (M_{env}) [M_{\odot}]	0.37	0.19	0.037	1×10^{-4}	2×10^{-5}
Envelope inner radius ($R_{e,min}$) [R_{\star}]	7.5	7.0	7.0	7.0	50.0
Envelope outer radius ($R_{e,max}$) [AU]	5000	5000	5000	500	500
Disk mass (M_{disk}) [M_{\odot}]	0.01	0.01	0.01	0.01	2×10^{-8}
Disk inner radius ($R_{d,min}$) [R_{\star}]	7.5	7.0	7.0	7.0	50.0
Disk outer radius ($R_{d,max}$) [AU]	50	200	300	300	300
Disk accretion rate (\dot{M}_{disk}) [$M_{\odot} yr^{-1}$]	2.8×10^{-8}	6.8×10^{-9}	4.6×10^{-9}	4.6×10^{-9}	0
Disk accretion luminosity ($L_{acc}(R_{d,min})$) [L_{\star}]	0.0069	0.0018	0.0012	0.0012	0
Cavity density [$n_{H_2} cm^{-3}$]	6.7×10^4	5.0×10^4	1.0×10^4	5.0×10^3	1.0×10^3
Cavity opening angle [deg]	10	20	30	90	90

create an ice-covered dust model for the envelope and midplane, the Maxwell-Garnett effective medium theory (Bohren & Huffman 1983) and the Mie theory were employed to calculate the absorption opacity, albedo (ω) and anisotropy parameter (g), as shown in Figure 2d-o for the outflow cavity, envelope, disk upper layer and disk midplane.

The position of the ices in the disk and envelope was defined via an interactive procedure by calculating the dust temperature using the Monte Carlo method. As the first approach, the dust temperature was calculated for all models, but without ice components. The calculated temperature was used to replace bare grains by covered grains, using the water desorption temperature. Since the new temperature distribution is different compared to the models using bare grains, the simulations were repeated until the temperature converges for values around 5% of difference between the prior and posterior calculations, as also done in Pontoppidan et al. (2005).

Three models of YSOs including ices are addressed in this paper. The virgin ice model describes a physical evolution without chemical evolution since the ices are not processed during the evolutionary sequence. 1st processing model assumes an ice mantle slightly processed by external Cosmic Rays (CRs), whereas the 2nd processing Model 3 is given by ices highly processed by CRs.

4.3. Density and Temperature profiles

Figure 3 show the temperature and density distribution for the evolutionary sequence between Class 0/I and Class III. The left panels in each box is a zoom-in of the right ones. The left box displays the density distribution that ranges between $10^{-18.5} - 10^{-19.5} g cm^{-3}$, i.e. $10^4 - 10^5 cm^{-3}$ in the Class 0/I and I and is extended

to large scales ($R_{out} = 5000$ AU). In Class II, this density variation is distributed in a disk scale until 300 AU. The right box shows the dust temperature distribution in each model, ranging from $T \sim 1000$ K nearby the central star to $T \sim 10-30$ K at the envelope region. At such a lower temperature, the outer envelope still cold enough to host ice-covered dust grains, which can be processed by the Interstellar Radiation Field (ISRF). For very embedded YSOs, the UV field might not dominate the synthesis of molecules, unless it is 40 times higher than the typical ISRF of the Interstellar Medium (Rocha & Pilling 2018). In that case, the chemistry is dominated by the low-temperature reaction, such as the cosmic ray induced processes.

In the disk region, the temperature in the midplane remains at around 15–20 K in all evolutionary stages due to UV shielding caused by the dust grains. In the upper disk layers, on the other hand, the temperature increases as the envelope mass decrease because the accretion process, and the temperature is around 100 K for Class I and 300 K for Class II at a radius of 100 AU. As a consequence, the major part of the Class I disk might host ices since the H_2O freeze-out occurs at temperatures below 150 K (Collings et al. 2004). The ice reservoir in Class II disks is therefore reduced compared to the previous evolutionary stage.

Figure 4 shows the dust temperature across the midplane for all the stages, and the H_2O freeze-out limit is indicated. The models show that water snowline moves inward until the Class II, and outwards for the Class III, which is in agreement with previous works (Kennedy & Kenyon 2008; Baillié et al. 2015), and would benefit the formation of giant planets at around 5 AU without significant migration. Quantitatively, Kennedy & Kenyon (2008) and Baillié et al. (2015) suggest that the water

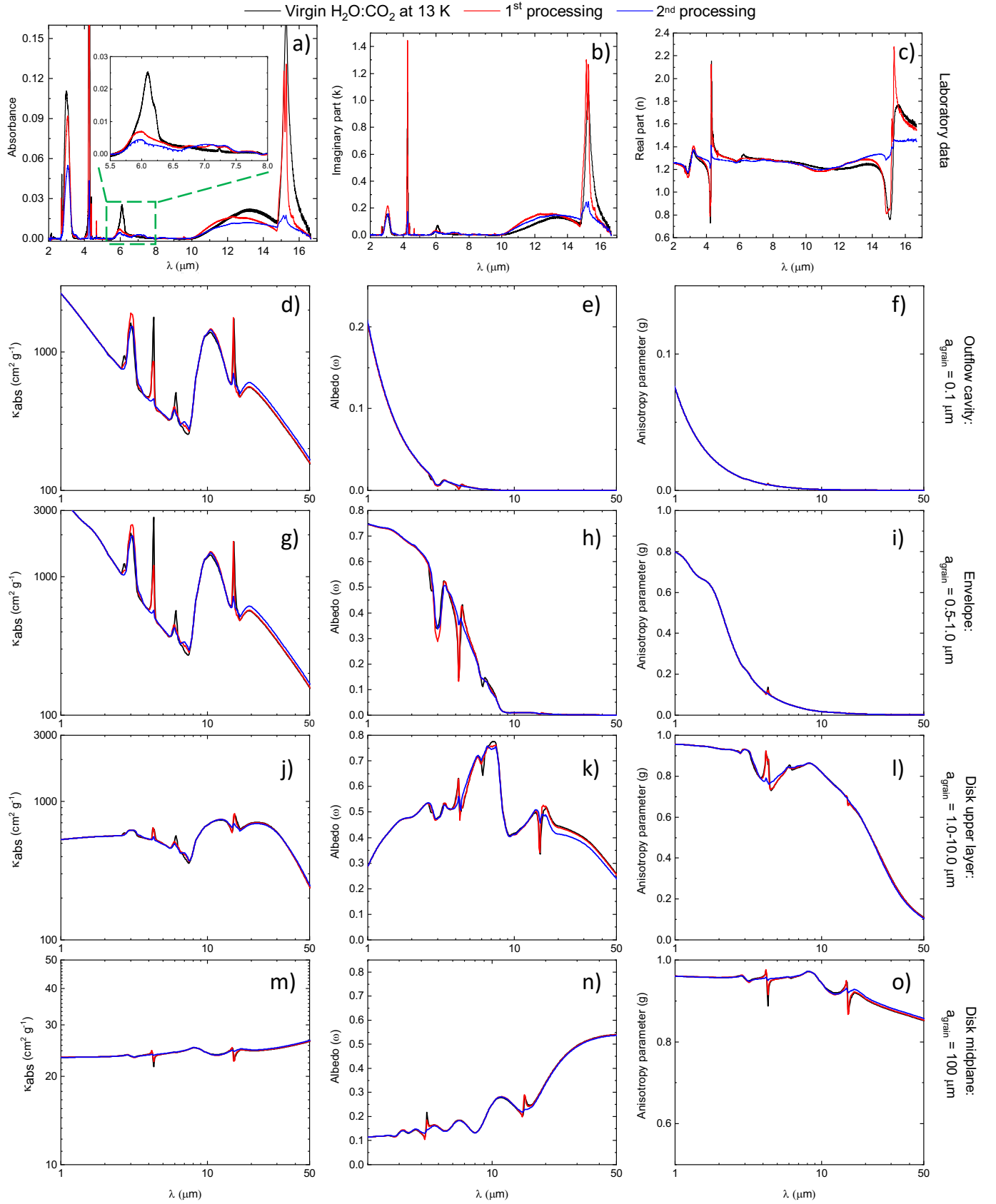


Figure 2. Laboratory data and opacity models. Panels a–c show the absorbance and the optical constants n and k at different fluences. The inner figures in panel a show different regions of the absorbance spectrum. Panels d–o show the dust parameters used in the models where the temperature is below 150 K, and for different regions in the YSOs (See details in the text).

snowline changes from 3.5 AU (Class 0/I) to 1.7 AU (Class II) and from 2.3 AU to 1.5 AU (same stages), respectively. In this work, the snowline is closer to the central star, compared to the previous models since it changes from 2 AU in Class 0/I to 0.9 AU in Class II. Despite the number difference, the same trend and the reduction by a factor of 2 are still observed. It worth to note, however, that snowlines might temporarily move outwards in the disk in a scenario of inside-out collapse (Zhang & Jin 2015; Cieza et al. 2016).

4.4. Spectral Energy Distributions

Figure 5 shows the SEDs of the simulated protostars at 10 inclination angles (i). Since we are looking at the ice features between 2.5–8.0 μm , a small range of wavelengths is shown, although the radiative transfer simulation was performed for $0.1\mu\text{m} \leq \lambda \leq 1000 \mu\text{m}$. In order to get the best signal-to-noise ratio due to the Monte Carlo noise in the simulation of dense regions, a number of 4×10^7 photons was used in the models. The SEDs show strong absorption bands which are associated to the H₂O ice (3 μm and 6 μm), CO₂ ice (4.27 μm) silicate (9.8 μm) and less noticeable in this scale shown, the contribution of complex molecules between 5.5–8.0 μm in the 1st and 2nd processing panels (see Figure 9). The silicate feature is seen in absorption for all inclinations in the Class 0/I stage, whereas it turns to an emission profile at a pole-on inclination in Class I due to the low optical depth to the source of emission. Such an emission profile is more pronounced for $i \leq 60^\circ$ at Class I/II since the envelope mass decreases by a factor of 5 from the previous to the new stage in these models. The ice profiles in the Class 0/I and Class I, are always observed in absorption at all inclinations. In the Class I/II, on the other hand, the ice absorption is only seen between $i = 20^\circ$ and $i = 60^\circ$. In extremely edge-on ($i = 80^\circ$ and $i = 90^\circ$) and face-on ($i = 20^\circ$ and $i = 10^\circ$) inclinations, the ice features are weak. It worth to note that the intensity of the ice absorption does not vary monotonically with the viewing angle, namely, from edge-on to face-on inclination as will be discussed in Section 5.

In addition to the SEDs, the continuum emission was also calculated for all 90 spectra described here. As discussed in Boogert et al. (2008), determining the best baseline is not trivial in real objects, and very accurate modelling is required to determine how the different regions of the disk or disk+envelope contribute to the continuum emission. In this paper, however, all SED components are known and were used to calculate the correct baseline for each model. For instance, Figure 6 show the continuum given by the dashed line for SEDs in

the model of virgin ices in Figure 5. The same procedure was employed for the models of 1st and 2nd processing.

5. RESULTS AND DISCUSSION

5.1. Ice optical depths

The Optical Depth (τ) for the models of virgin and processed ices, related to H₂O ice ($\sim 3 \mu\text{m}$), CO₂ ice ($\sim 4.27 \mu\text{m}$) and the complex molecules between 5.5–7.5 μm were calculated at 10 inclinations between face-on and edge-on angles using the equation described in Section 2. Figures 7, 8 and 9 show the ice features for each case. The optical depth variation with inclination is due to the relation between optical depth and density along the line of sight. One can note from Equation 5 that ρ_{env} decreases with the radius r , but also with the $\cos(\theta)$, namely, from the midplane toward the cavity region. Since the optical depth is given by $d\tau = -\kappa\rho\cos\theta ds$, where κ is the opacity, ρ the density and ds is the optical path, $d\tau$ decreases if ρ_{env} also does. Furthermore, the small variation observed in Class 0/I compared to Class I and Class I/II is due to the negligible envelope density variation with the polar angle for small cavity apertures. In Class I and Class I/II, however, the ice optical depth does not vary monotonically between $i = 90^\circ$ and $i = 60^\circ$. It is evident that the inclination of $i = 70^\circ$ shows the deepest ice bands due to a geometric effect as previously shown by Pontoppidan et al. (2005). Due to the large optical depth through the midplane, the IR source at edge-on inclination is dominated by a small fraction of scattered infrared photons toward high angles. However, at an inclination above the disk opening angle, the stellar emission itself dominates and the entire envelope is probed, leading to deepest ice bands in the spectrum. Below $i = 70^\circ$ in the models shown in this paper, the ice column density decreases monotonically until pole-on inclinations.

The H–O stretching vibrational mode seen in Figure 7 between 2.7 and 3.6 μm is usually reported in YSOs as containing a red wing at longer wavelengths caused by scattering on large ice-coated grains (Boogert et al. 2000) and the absorption by ammonia hydrates (Hagen et al. 1983). The absence of this effect in the synthetic spectra does not argue in favour of any of these two cases since neither large grains or N-containing species were included in the ice-dust model for the envelope. It is also true that this water vibrational mode shows evidence of crystallization if the ice is heated above 100 K. However, as noticed from Figure 2a, the CR-processing is not enough to induce discernible structural changes in the ice matrix as seen from the IR spectrum.

In Figure 8, the C–O stretching mode of CO₂ ice at around 4.27 μm is shown. As discussed in Boogert

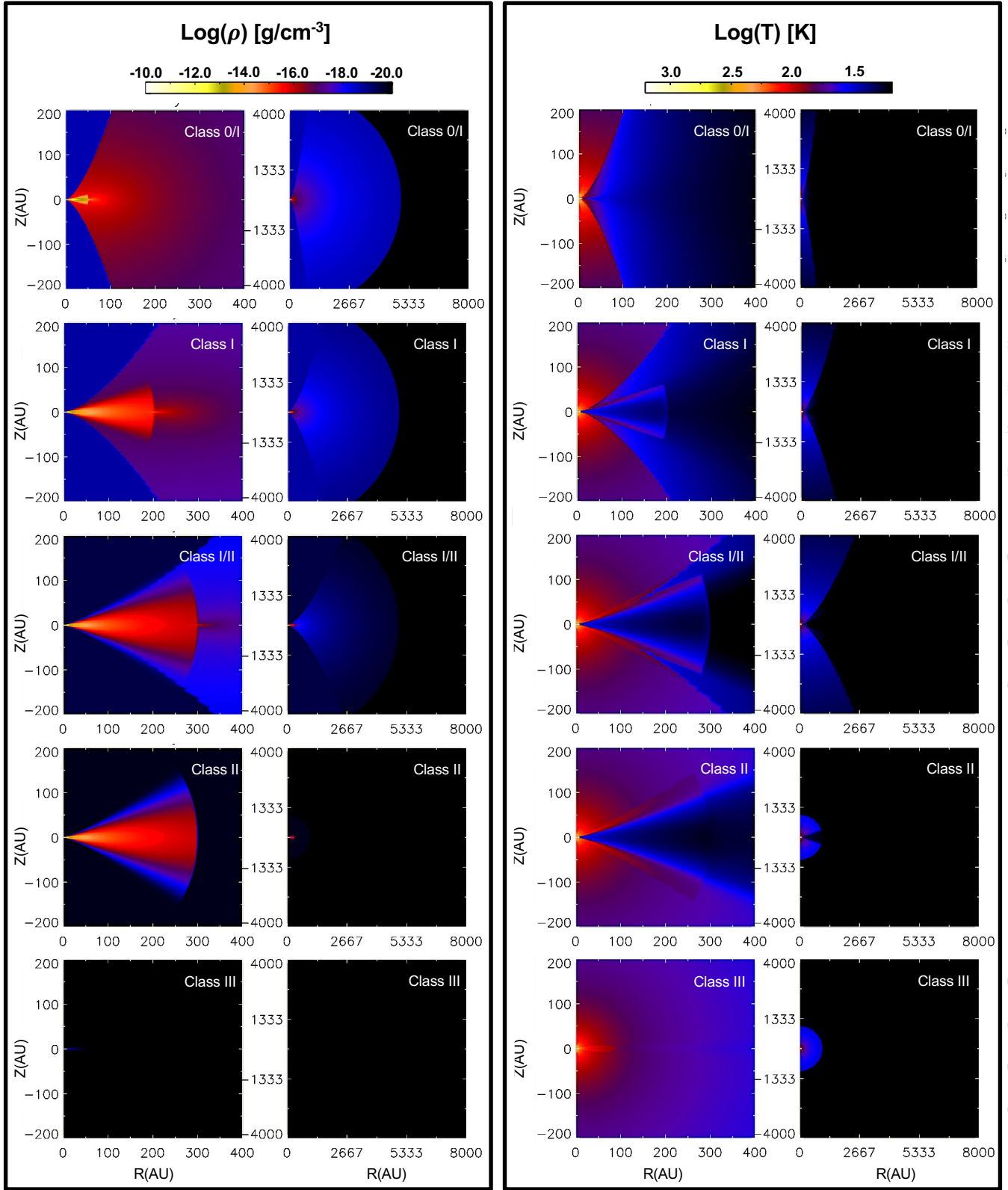


Figure 3. Temperature and density profile calculated with the radiative transfer code for the Class 0/I - III. The colours are shown in logarithmic scale and the values are indicated by the bar on the top. Z and R are, respectively, the radial and vertical scale, both given in astronomical units (AU). For each box, the left models are a zoom-in of the right ones.

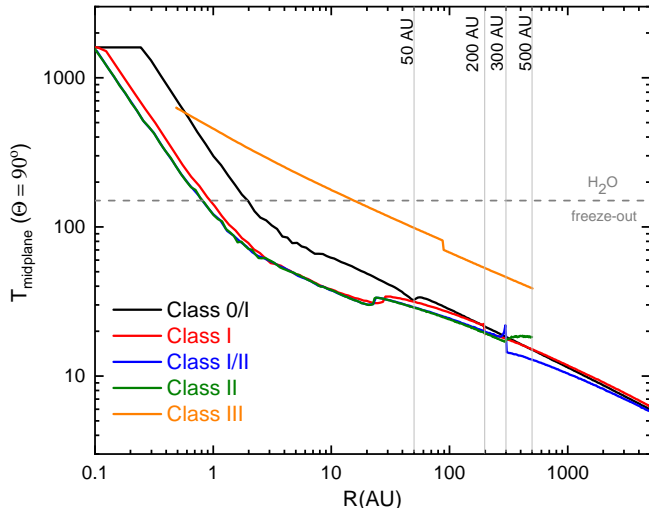


Figure 4. Radial dust temperature at $\theta = 90^\circ$ of the models in different stages, as indicated by the colour scheme. The water freeze-out line is also shown by the dashed grey line. The vertical grey lines indicate the outer radius of the disk (50 AU, 200 AU, 300 AU) and the outer envelope radius in evolved stages (500 AU).

et al. (2002a); Ehrenfreund et al. (2001) the position and width of this peak changes with the grain geometry and its fraction in the ice matrix. As pointed out by Ehrenfreund et al., this vibrational mode presents a narrow profile if less abundant in a polar matrix compared to the pure ice. For instance, the fraction of 14% of CO_2 ice in a H_2O matrix fits better the CO_2 band at $4.27 \mu\text{m}$ for the Class I YSO Elias 29 compared to the pure CO_2 ice adopted by Rocha & Pilling (2015). The CO_2 analysis at $\sim 15 \mu\text{m}$ from Spitzer observations (Pontoppidan et al. 2008) has strongly suggested that 2/3 of the CO_2 absorption features is due to carbon dioxide ice diluted in H_2O ice, whereas 1/3 is likely due to $\text{CO}:\text{CO}_2$ mixture. Ehrenfreund et al. (1997) shows a narrowing of the CO_2 absorption feature if mixed in CO ice at fractions below 26%. As a consequence, if the band strength (\mathcal{A}) is kept constant, this effect would lead to lower column density values since it depends on the integrated optical depth as seen in Equation 2. Nevertheless, this is hard to verify since the \mathcal{A} for CO_2 diluted in CO ice is unknown.

Figure 9 shows the optical depth between $5.5\text{--}7.5 \mu\text{m}$ that usually is associated with the presence of Complex Organic Molecules such as HCOOH , CH_3OH , CH_3CHO , $\text{CH}_3\text{CH}_2\text{OH}$ (Schutte et al. 1996; Gibb et al. 2000; Keane et al. 2001; Boogert et al. 2008, 2015). In this work, we highlight the contribution of methanol and formic acid at $6.75 \mu\text{m}$ and $7.24 \mu\text{m}$, respectively, as a result of the ice processing by cosmic rays. Addressing the ice components in this spectral range is rather dif-

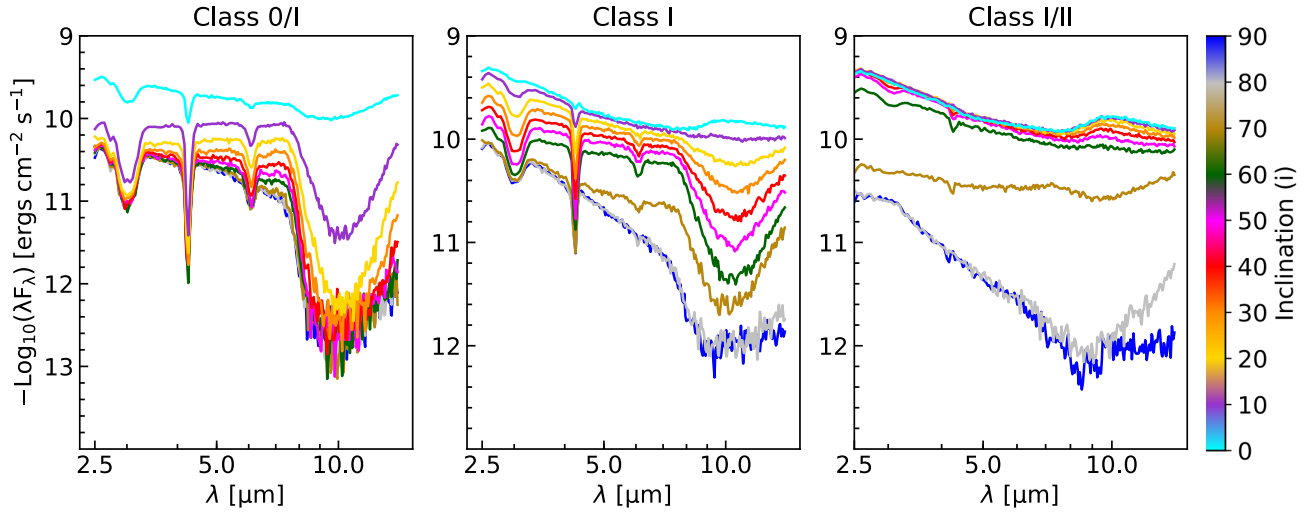
ficult since the IR profile of complex molecules changes with the chemical environment inside the ice matrix. Boogert et al. (2008) suggests a decomposition method by removing the pure water contribution, and fitting the residual with 5 independent absorption components obtained from the combination of different YSO spectra. Each component might have multiple carriers due to blended vibrational modes, as for example CH_3OH and NH_4^+ at $6.85 \mu\text{m}$. In this paper, however, a simple Gaussian decomposition of the spectrum by using 5 components is employed in order to isolate the contribution of CH_3OH and HCOOH , whose the position in spectra are shown in Pilling et al. (2010). The Appendix A shows the Gaussian decomposition method, where the components due to CH_3OH and HCOOH ice are shown.

5.2. Synthetic column density and the spectral index

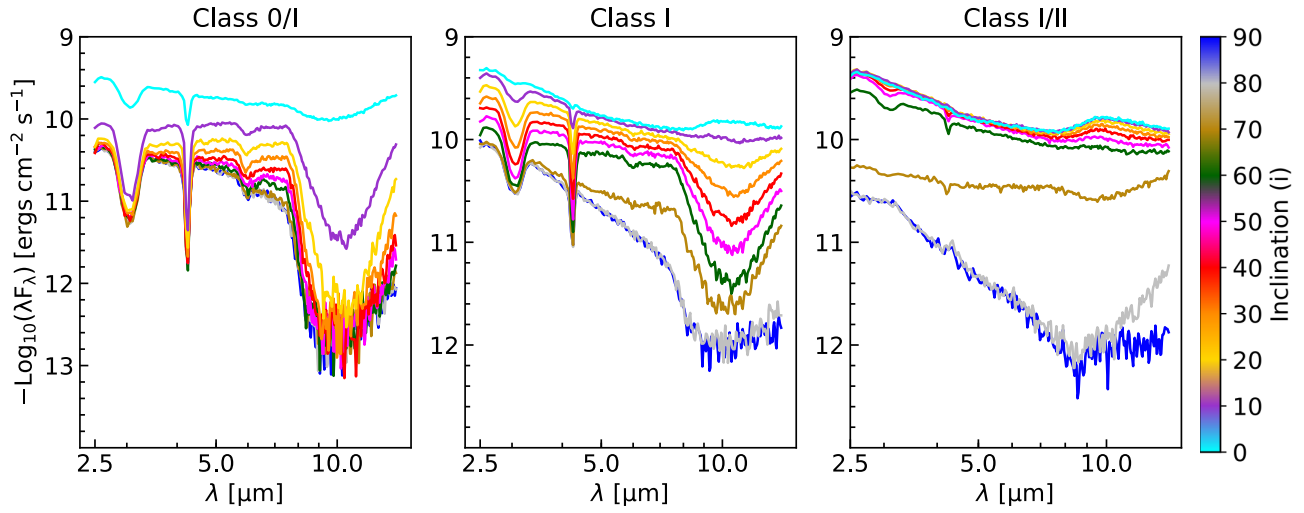
In order to avoid blending effects, the H_2O and CO_2 column densities were calculated from the bands at $3 \mu\text{m}$ and $4.27 \mu\text{m}$ shown in Figures 7-9, using Equation 2. In the case of CH_3OH ($6.85 \mu\text{m}$) and HCOOH ($7.25 \mu\text{m}$), the spectral decomposition method described in Appendix A was used. The band strength adopted for each vibrational mode were: $\mathcal{A}_{\text{H}_2\text{O}} = 2.6 \times 10^{-16} \text{ cm molecule}^{-1}$, (Hagen et al. 1981), $\mathcal{A}_{\text{CO}_2} = 7.6 \times 10^{-17} \text{ cm molecule}^{-1}$ (Gerakines et al. 1995), $\mathcal{A}_{\text{HCOOH}} = 1.5 \times 10^{-17} \text{ cm molecule}^{-1}$ (Park & Woon 2006), and $\mathcal{A}_{\text{CH}_3\text{OH}} = 1.2 \times 10^{-17} \text{ cm molecule}^{-1}$ (Hudgins et al. 1993). This paper assumes a constant \mathcal{A} for the 3 models, although the band strength is a sensitive physico-chemical parameter to the ice composition. As shown by Öberg et al. (2007), the band strength of the H_2O bulk stretch at $3 \mu\text{m}$ drops linearly in $\text{H}_2\text{O}:\text{CO}_2$ ice mixture, compared to the pure H_2O . However, in the scenario of energetic processing, where several species are formed, determining an accurate band strength still an open problem in astrochemistry.

Figure 10 shows the synthetic column density (N) of the ices X : H_2O , CO_2 , CH_3OH and HCOOH as a function of the spectral index calculate for the model of virgin ices, 1st processing and 2nd processing shown by the filled circles, squares and triangles, respectively. The colours indicate the inclination angle as given by the colorbar at the bottom of the figure. The virgin ice model represents a scenario where the ice column density varies only due to the envelope dissipation and angle inclination. The two processing models, on the other hand, simulate a case where the ice column density decreases due to the physical effects in the virgin ice model, as well as due to the ice energetic processing. Due to the ambiguity in the envelope mass with the spectral index shown by Crapsi et al. (2008), the spectral index (α)

Virgin ice



1st processing



2nd processing

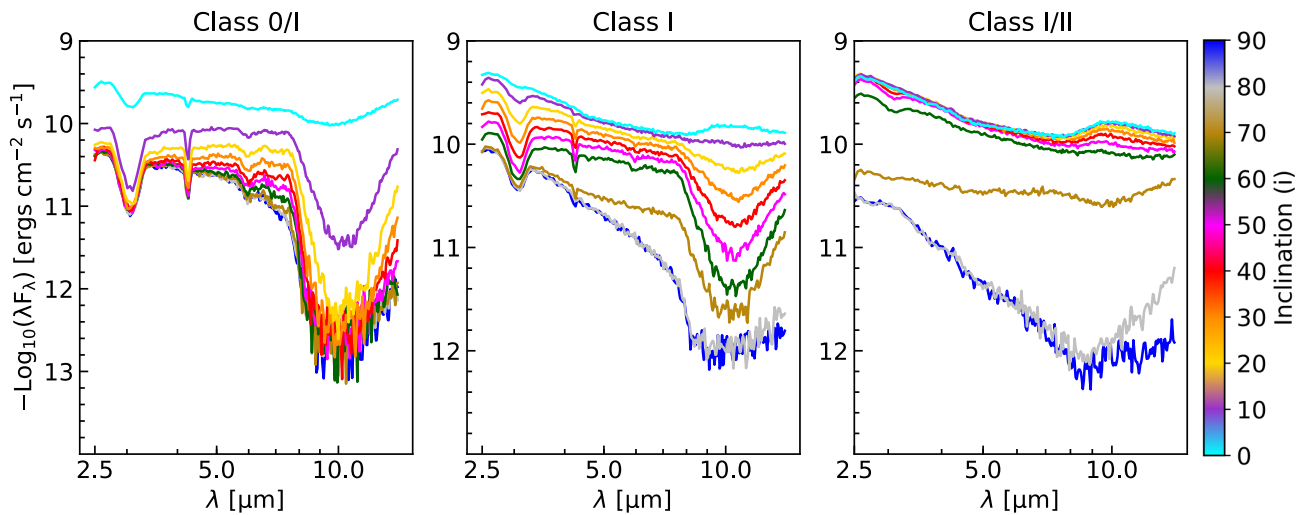


Figure 5. Spectral Energy Distribution of the YSOs simulated in this paper for the Class 0/I–I/II at three levels of ice processing and 10 inclinations.

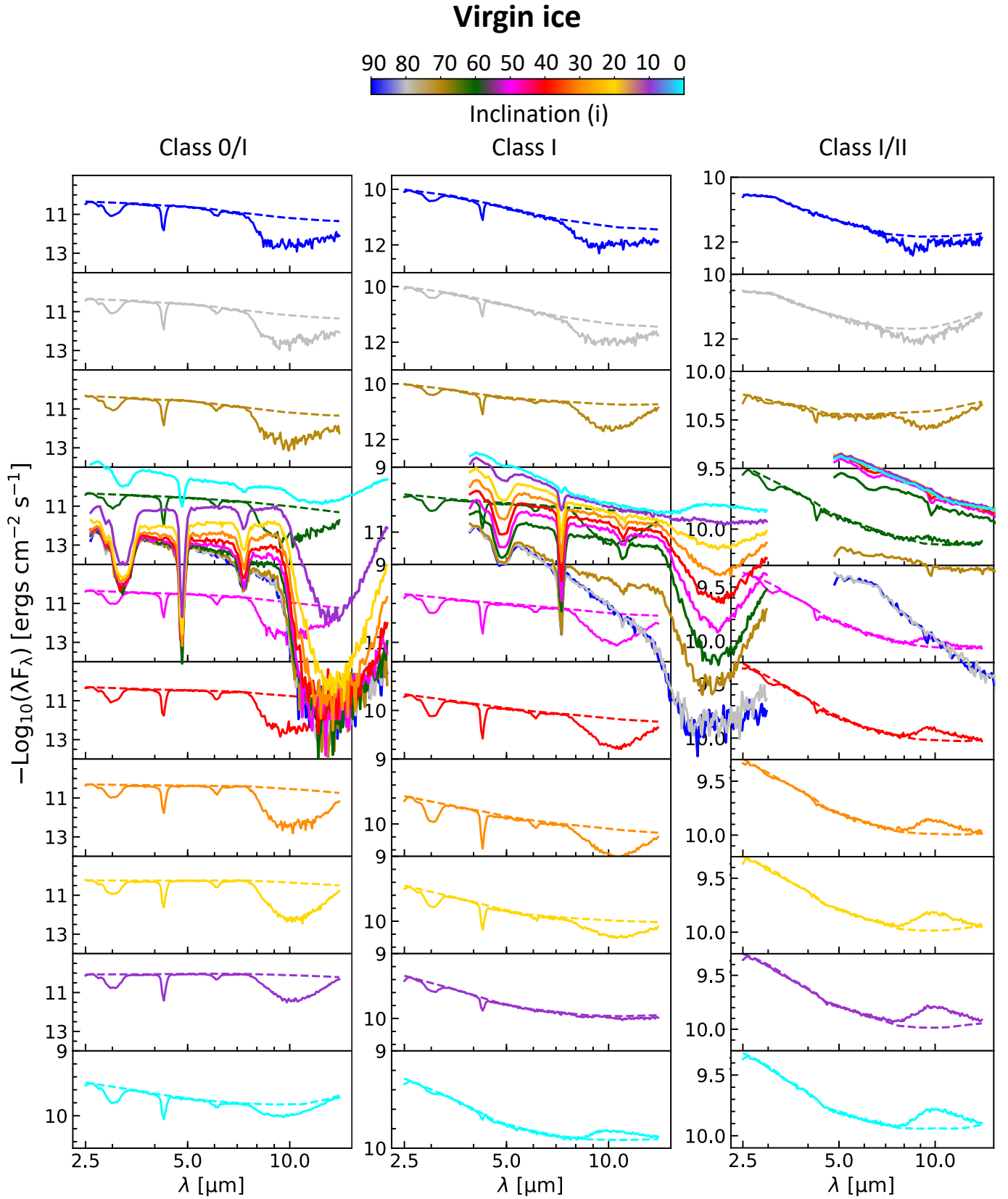


Figure 6. Spectral Energy Distribution for the model of virgin ices, where the continuum line is also indicated by the dashed lines. The colours indicate the inclinations.

Virgin ice

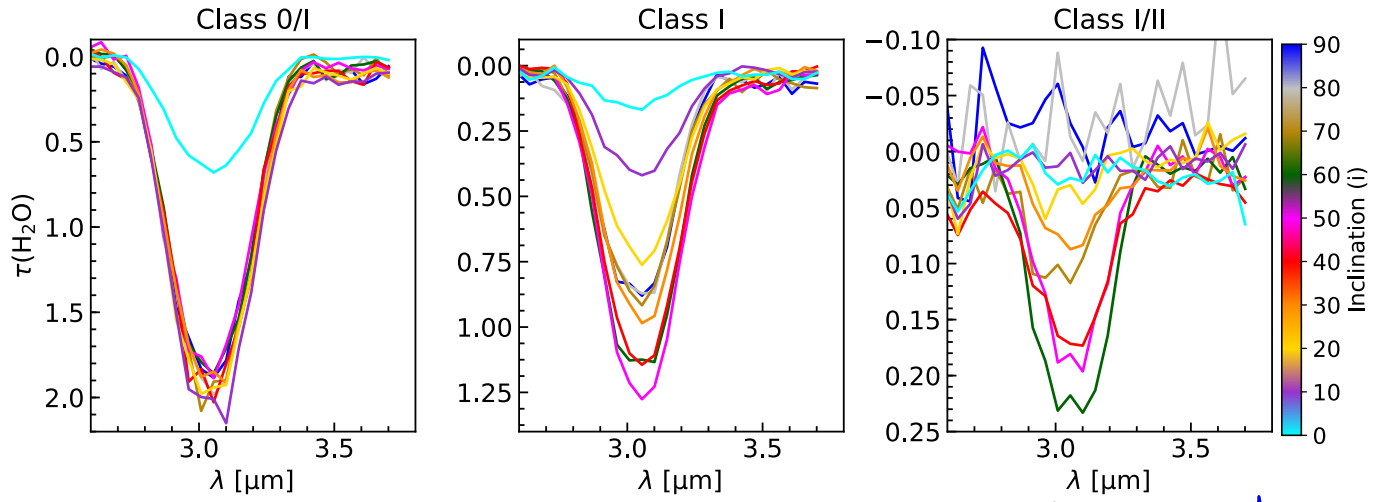
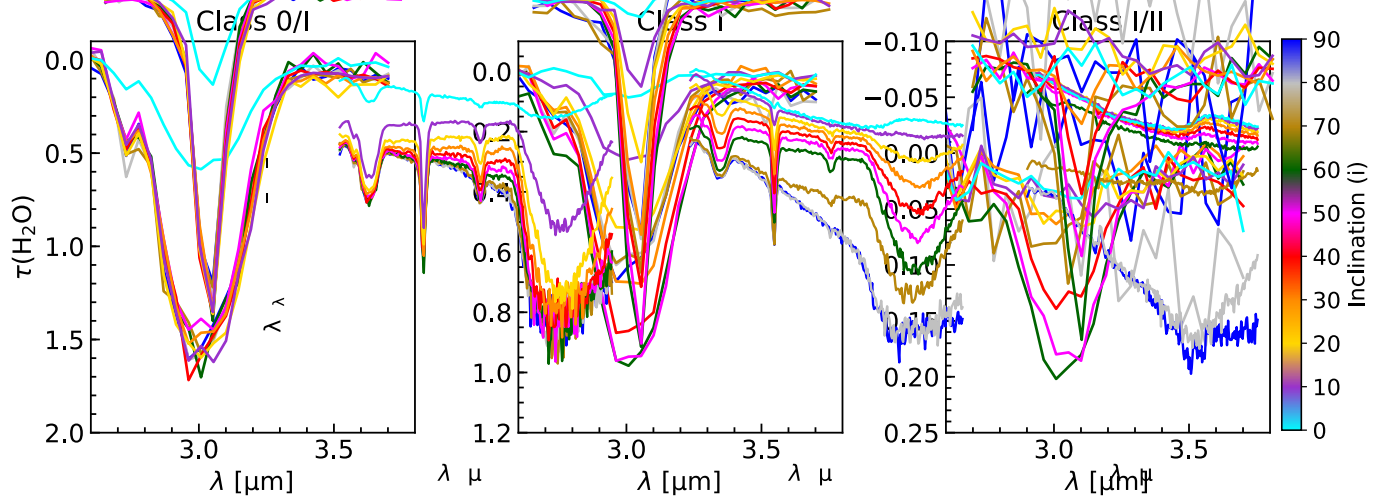
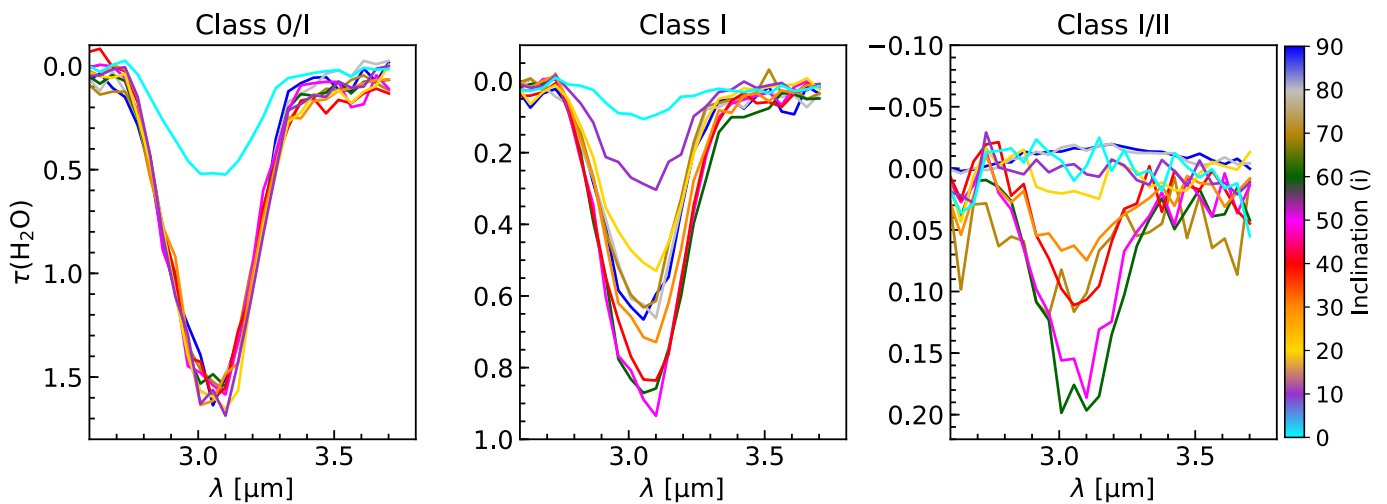
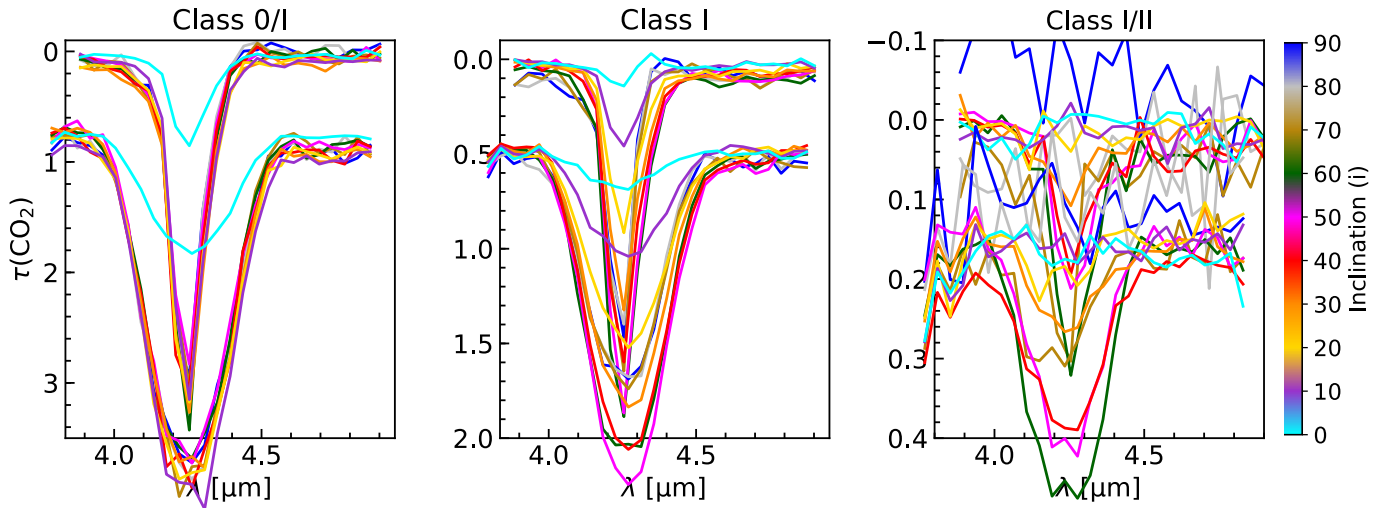
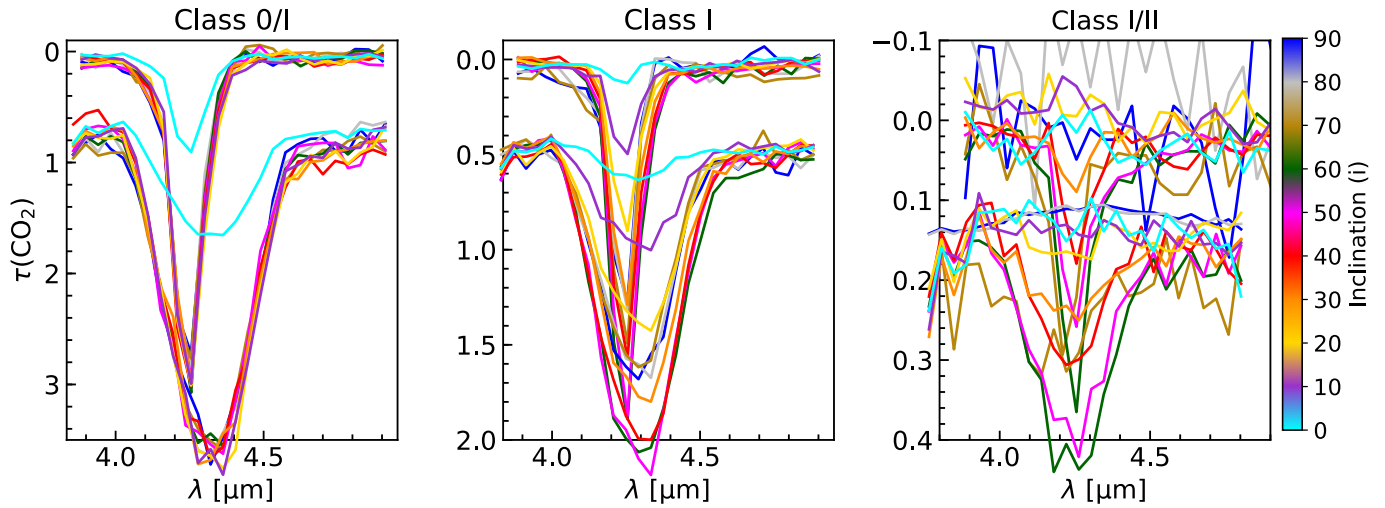
1st processing2nd processing

Figure 7. Optical depth of H_2O ice at around $3 \mu\text{m}$ shown for the Class 0/I–I/II at three levels of ice processing and 10 inclinations as indicated by the colour bar.

Virgin ice



1st processing



2nd processing

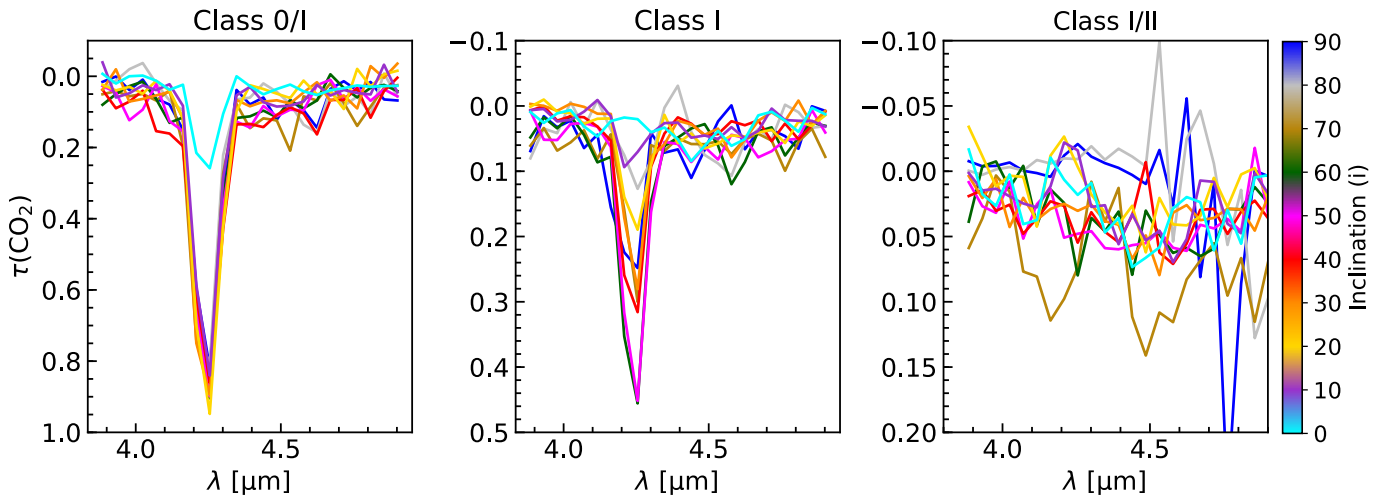


Figure 8. Optical depth of CO₂ ice at around 4.27 μm shown for the Class 0/I–I/II at three levels of ice processing and 10 inclinations as indicated by the colour bar.

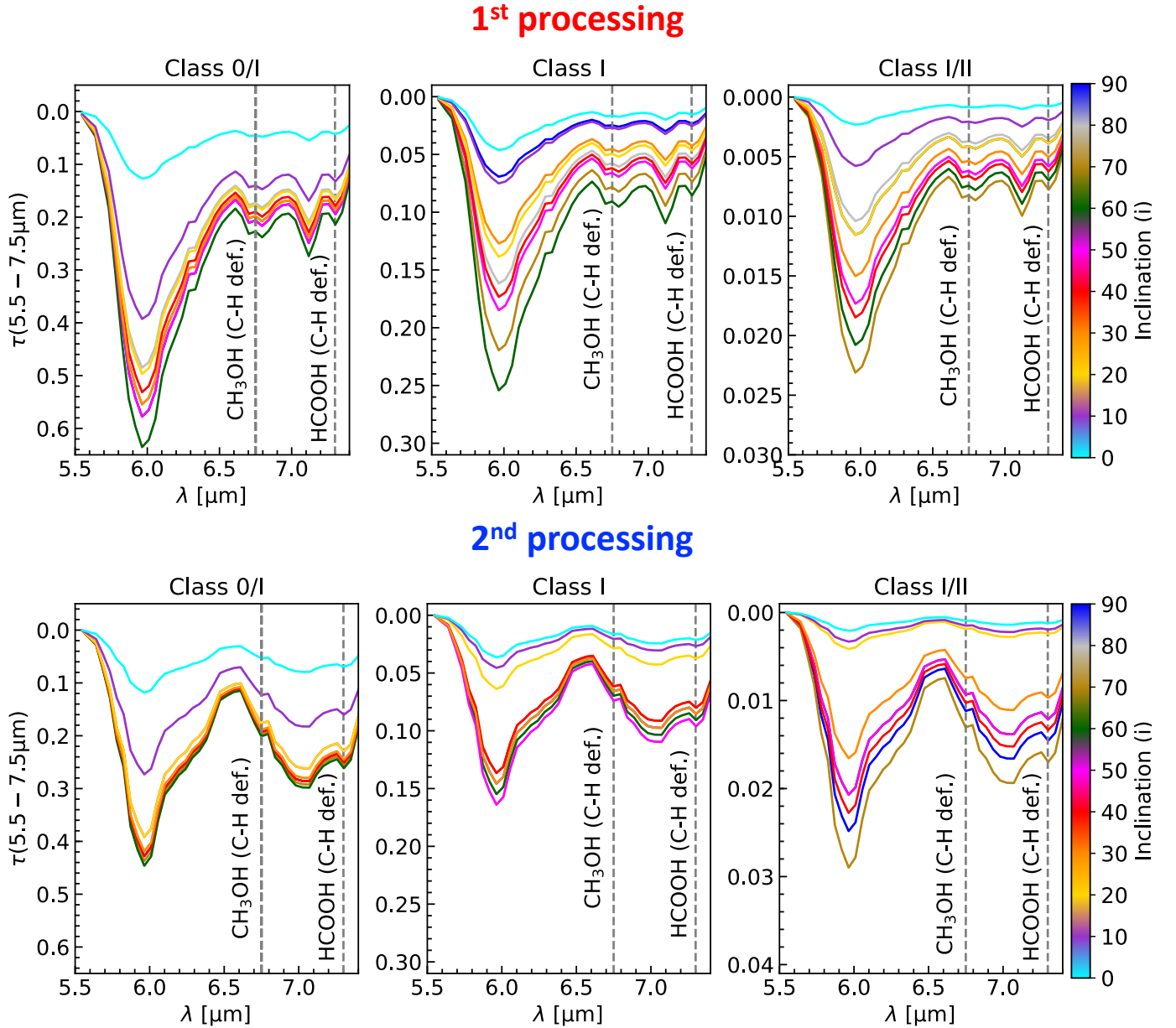


Figure 9. Optical depth between 5.5–7.5 μm shown for the Class 0/I–I/II at two levels of ice processing and 10 inclinations as indicated by the colour bar. The contributions of CH_3OH and HCOOH are indicated by the vertical and grey dashed lines at 6.75 μm and 7.24 μm , respectively.

to characterize the evolutionary stage of YSOs in this paper is kept constant for each evolutionary stage and processing level. For Class 0/I, the adopted α values are 2.8, 2.6 and 2.4 for the virgin ice, 1st and 2nd processing, respectively. The small offset is only to allow better readability. At Class I, the α values are 1.4, 1.1 and 0.9, whereas for Class I/II, it is assumed 0.2, 0, -0.2. In this way, Figure 10 shows the comparison between model and observation from the perspective of the inclination angle and ice processing level. As pointed-out in Section 4.4, the ice column density does not vary monotonically with the 10 inclination angles shown in

Figure 10. The maximum N_X occurs for $60^\circ \leq i \leq 70^\circ$, whereas the minimum N_X corresponds to 0° . The observational fit and the confidence intervals taken from Figure 1 are shown by the solid and dashed green lines, respectively. The grey, red and blue shaded areas cover the ice column density dispersion for the three models used in this paper according to the spectral index.

Figure 10a shows that, except for the pole-on inclination angle, the H_2O column densities predicted by the three models lie inside the confidence interval of the observational fit at the stage of Class 0/I objects. However, the inclination effect and ice processing can-

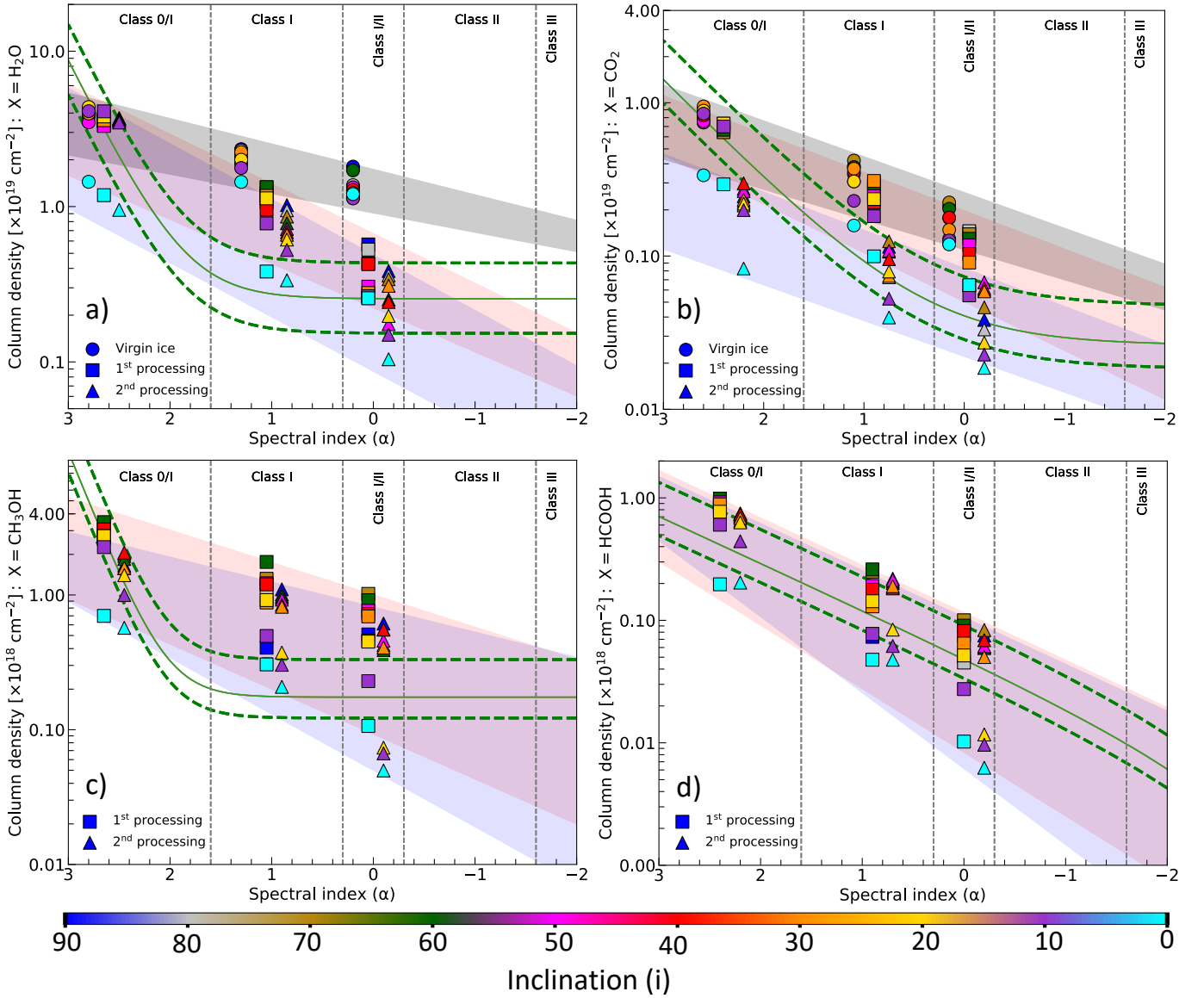


Figure 10. Plot containing the spectral index against the column density of the ices H_2O , CO_2 , CH_3OH and HCOOH calculated from the models of virgin and processed ices. The three levels of ice processing are indicated by the filled circles, squares and triangles, respectively. The inclination effect is shown by the color scheme given by the colorbar. Each evolutionary stage is indicated by the top labels. The solid and dashed green lines correspond to the exponential fit and confidence intervals in Figure 1. The grey, red and blue shaded regions cover column density dispersion for all inclination according to the spectral index.

not explain the vertical spread of two orders of the magnitude observed at this stage. Even though the pole-on column densities are 50–70% lower than the highest inclinations, they are still unable to explain the entire vertical variation. A likely cause of this wide vertical spread in the same evolutionary stage is the initial envelope mass variation associated with protostars at early stages, since that, at the same physical conditions, lower envelope mass leads to a lower ice column density. At the Class I stage, all the 3 models overestimate the water ice column density, except for the pole-on inclina-

tion, which suggests that H_2O is destroyed by mechanisms other than cosmic rays radiolysis ($\text{H}_2\text{O} + \text{CR} \rightarrow \text{OH} + \text{H}$), such as photolysis induced by UV and X-rays. At Class I/II stage, on the other hand, only the virgin ice model overestimate the H_2O ice column density, whereas the 1st and 2nd processing model are in agreement with the observation. Nevertheless, it is inconclusive that such a result is related to the physical and chemical evolution of the protostar since only one stage of evolution fit the data.

The trends shown by the shaded areas in Figure 10a indicate a slow N_{ice} decreasing at early stages and the absence of the *plateau* for late stages when compared to the observational data. While the fast decreasing observed at early stages for water ice is likely related to other destruction mechanisms not included in this paper, the absence of *plateau* at late stages can suggest that, at least 30% of the observed ices lying outside the protostar itself, and therefore, not affected by the accretion process, might contribute to keeping the observed ice column density fraction roughly constant as shown by Pontoppidan et al. (2005), Boogert et al. (2000) and (Aikawa et al. 2012).

In the case of the N_{CO_2} variation shown in Figure 10b, the virgin ice and the 1st processing models provides column densities inside the observational confidence interval in Class 0/I. The CO_2 destruction in the 2nd processing model, on the other hand underestimate N_{CO_2} . Nevertheless, in the more evolved stages, namely, Class I and Class I/II, the 2nd processing model predicts CO_2 ice column densities inside the confidence interval, whereas the virgin ice and the 1st processing models, generally overestimate the column densities. As in the case of H_2O ice, the effect of the physical and chemical evolution of protostars cannot be confirmed. The decreasing trends shown by the shaded areas also indicate the absence of the *plateau* at late stages. For the Class I YSOs, Elias 29 and CRBR2422.8–3423, the estimated column density in foreground clouds are $N_{\text{CO}_2} \sim 2 \times 10^{17} \text{ cm}^{-2}$ (Boogert et al. 2000) and $N_{\text{CO}_2} \leq 6 \times 10^{17} \text{ cm}^{-2}$ (Pontoppidan et al. 2005), respectively.

Figure 10c shows the variation of the methanol ice column density against the spectral index as calculated from the band at $6.85 \mu\text{m}$ spectral feature. One can note that the methanol column densities calculated from 1st and 2nd processing models mostly lie inside the observational range for Class 0/I, although the vertical spread is not explained, whereas it is overestimated in the later stages. The reason of the overestimation is likely due to (i) the high efficiency of CH_3OH production because of the large CO_2 fraction in the experiments and (ii) due to the decomposition method itself. In the latest case, Boogert et al. (2008) the component attributed to CH_3OH ice has a full width at half maximum (FWHM) 50% lower than the assumed in this paper, which would lead to a lower column density calculation. Taking this difference into account, if the FWHM Gaussian component associated with methanol in this paper, is reduced in 50%, it would represent an ice column density 20% lower. Such a reduction, however, would not provide a better agreement between observation and model. In summary, the model fails to reproduce the methanol ice

column density variation and the fast decreasing compared to the other molecules as pointed-out at the beginning of the paper. Further investigation must be carried out for this case, and other laboratory ice samples can be used instead, as well as how the methanol formation is affected during the protostellar collapse.

HCOOH ice column density variation is shown in Figure 10d as calculated from the absorption feature at $7.24 \mu\text{m}$. Both 1st and 2nd processing models provide N_{HCOOH} inside the observational confidence interval in most of the cases. The good agreement between observation and the two models suggest that the lower decreasing rate of formic acid is mainly due to the envelope dissipation by accretion than due to the energetic processing of the ice i.e. chemical evolution. The absence of the *plateau* at late stages, on the other hand, indicate that, if it is caused by ices in foreground clouds, then its abundance quiescent molecular clouds is very low.

In summary, the evolutionary models along with the ice samples used in this paper, in general, do not explain the observed trends of ice column density with the evolutionary stage, with the exception of HCOOH . Further investigations addressing different physical parameters and ice mixtures must be used in order to explain the observational data.

6. CONCLUSIONS

This paper shows the correlation between the ice column densities of H_2O , CO_2 , CH_3OH and HCOOH and spectral index (α) of 27 early-stage YSOs. A computational simulation combining 2D radiative transfer model and laboratory data of virgin and processed ices was carried-out to study the ice column density decreasing from early to late stages of the protostellar evolution. The conclusions are summarized below:

1. The observational data suggest that ice column densities are correlated with the spectral index from Class 0/I to Class I/II. Additionally, it is observed that H_2O and CH_3OH ices reach an ice column density *plateau* at Class I whereas for CO_2 ice, the *plateau* is reached at Class I/II. In the case of HCOOH , however, it is not observed. If an exponential function is assumed to fit the data, it is found that CH_3OH ice decreases faster than the other ices, whereas HCOOH decreases slowly.
2. In agreement with previous works, the models simulated in this paper, shows that the H_2O snow line moves inward from 2 AU at Class 0/I to 0.7 AU at Class II. During the evolution to Class III, the snowline moves outward to 20 AU. Nevertheless, the region where the ices are located is optically

thick in the mid-IR, and therefore the absorption seen in the spectra are due to the ices located in the envelope. As a consequence of the density distribution in the Class 0/I to Class I/II, the ice column density does not vary monotonically with the inclination angle (i). The highest column density is, generally, seen for $i \sim 20^\circ$ at Class 0/I and $i \sim 60^\circ$ at Class I.

3. The computational models show that the combination of physical evolution (envelope dissipation), chemical evolution (ice processing) and inclination angle effect is able to reproduce the N_{HCOOH} decreasing with the spectral index. However, in the case of H_2O , CO_2 and CH_3OH , the models fail to reproduce the observations in all evolutionary stages. Additionally, other destruction pathways not included in the current method must be addressed to understand why water and methanol ice column density decrease faster than CO_2 and HCOOH .
4. The absence of the ice column density *plateau* in the models suggest that there is fraction of ice ab-

sorption located in foreground clouds in order to explain the observations. More accurate models including other physical and chemical effects not addressed in this paper could confirm or reject this hypothesis. From the observational perspective, ices in foreground clouds have been already presented in the literature indicating values close to the ice column density *plateau* estimated in this paper for H_2O and CO_2 .

The authors acknowledge the careful revision of the anonymous referee that improved the quality of this paper. WRMR thanks the São Paulo Research Foundation - FAPESP (grant# PD2015/10492-3, BEPE2016/23054-7) for the financial support of this work and also FVE/UNIVAP. The research of WRMR also acknowledges support from the European Research Council (ERC) under the European Union's Horizon 2020 research and innovation programme through ERC Consolidator Grant "S4F" (grant agreement No 646908). SP thanks FAPESP (grant# BEPQ2016/22018-7), FVE, CAPES and CNPq.

REFERENCES

- Agúndez, M., & Wakelam, V. 2013, *Chemical Reviews*, **113**, 8710
- Aikawa, Y., Kamuro, D., Sakon, I., et al. 2012, *A&A*, **538**, A57
- Allamandola, L. J., Sandford, S. A., & Valero, G. J. 1988, *Icarus*, **76**, 225
- Andersen, B. C., Stephens, I. W., Dunham, M. M., et al. 2019, *ApJ*, **873**, 54
- Andre, P., Ward-Thompson, D., & Barsony, M. 1993, *ApJ*, **406**, 122
- Baillié, K., Charnoz, S., & Pantin, E. 2015, *A&A*, **577**, A65
- Boduch, P., Dartois, E., de Barros, A. L. F., et al. 2015, in *Journal of Physics Conference Series*, Vol. 629, *Journal of Physics Conference Series*, 012008
- Bohren, C. F., & Huffman, D. R. 1983, *Absorption and scattering of light by small particles*
- Boogert, A. C. A., Blake, G. A., & Tielens, A. G. G. M. 2002a, *ApJ*, **577**, 271
- Boogert, A. C. A., Gerakines, P. A., & Whittet, D. C. B. 2015, *ARA&A*, **53**, 541
- Boogert, A. C. A., Hogerheijde, M. R., Ceccarelli, C., et al. 2002b, *ApJ*, **570**, 708
- Boogert, A. C. A., Tielens, A. G. G. M., Ceccarelli, C., et al. 2000, *A&A*, **360**, 683
- Boogert, A. C. A., Pontoppidan, K. M., Knez, C., et al. 2008, *ApJ*, **678**, 985
- Caselli, P., & Ceccarelli, C. 2012, *A&A Rv*, **20**, 56
- Cieza, L. A., Casassus, S., Tobin, J., et al. 2016, *Nature*, **535**, 258
- Collings, M. P., Anderson, M. A., Chen, R., et al. 2004, *MNRAS*, **354**, 1133
- Crapsi, A., van Dishoeck, E. F., Hogerheijde, M. R., Pontoppidan, K. M., & Dullemond, C. P. 2008, *A&A*, **486**, 245
- de Valon, A., Dougados, C., Cabrit, S., et al. 2020, *A&A*, **634**, L12
- Drury, L., Ellisson, D., & Meyer, J.-P. 2000, *Nuclear Physics A*, **663**, 843c
- Ehrenfreund, P., Boogert, A. C. A., Gerakines, P. A., Tielens, A. G. G. M., & van Dishoeck, E. F. 1997, *A&A*, **328**, 649
- Ehrenfreund, P., d'Hendecourt, L., Charnley, S., & Ruitkamp, R. 2001, *J. Geophys. Res.*, **106**, 33291
- Fuchs, G. W., Cuppen, H. M., Ioppolo, S., et al. 2009, *A&A*, **505**, 629
- Garrod, R. T., & Herbst, E. 2006, *A&A*, **457**, 927
- Gerakines, P. A., Schutte, W. A., Greenberg, J. M., & van Dishoeck, E. F. 1995, *A&A*, **296**, 810

- Gibb, E. L., Whittet, D. C. B., Boogert, A. C. A., & Tielens, A. G. G. M. 2004, *ApJS*, 151, 35
- Gibb, E. L., Whittet, D. C. B., Schutte, W. A., et al. 2000, *ApJ*, 536, 347
- Greene, T. P., Wilking, B. A., Andre, P., Young, E. T., & Lada, C. J. 1994, *ApJ*, 434, 614
- Hagen, W., Tielens, A. G. G. M., & Greenberg, J. M. 1981, *Chemical Physics*, 56, 367
- . 1983, *A&A*, 117, 132
- Henning, T., & Semenov, D. 2013, *Chemical Reviews*, 113, 9016
- Herbst, E., & van Dishoeck, E. F. 2009, *ARA&A*, 47, 427
- Hudgins, D. M., Sandford, S. A., Allamandola, L. J., & Tielens, A. G. G. M. 1993, *ApJS*, 86, 713
- Indriolo, N., & McCall, B. J. 2013, *Chem. Soc. Rev.*, 42, 7763
- Jørgensen, J. K., van Dishoeck, E. F., Visser, R., et al. 2009, *A&A*, 507, 861
- Keane, J. V., Tielens, A. G. G. M., Boogert, A. C. A., Schutte, W. A., & Whittet, D. C. B. 2001, *A&A*, 376, 254
- Kennedy, G. M., & Kenyon, S. J. 2008, *ApJ*, 673, 502
- Lada, C. J. 1987, in *IAU Symposium*, Vol. 115, *Star Forming Regions*, ed. M. Peimbert & J. Jugaku, 1
- Lada, C. J., & Wilking, B. A. 1984, *ApJ*, 287, 610
- McLean, I. S., Becklin, E. E., Bendiksen, O., et al. 1998, in *Proc. SPIE*, Vol. 3354, *Infrared Astronomical Instrumentation*, ed. A. M. Fowler, 566
- Moorwood, A. F. 1997, in *Proc. SPIE*, Vol. 2871, *Optical Telescopes of Today and Tomorrow*, ed. A. L. Ardeberg, 1146
- Mottram, J. C., van Dishoeck, E. F., Kristensen, L. E., et al. 2017, *A&A*, 600, A99
- Öberg, K. I. 2016, *Chemical Reviews*, 116, 9631, PMID: 27099922
- Öberg, K. I., Boogert, A. C. A., Pontoppidan, K. M., et al. 2011, *ApJ*, 740, 109
- Öberg, K. I., Fraser, H. J., Boogert, A. C. A., et al. 2007, *A&A*, 462, 1187
- Padgett, D. L., Brandner, W., Stapelfeldt, K. R., et al. 1999, *AJ*, 117, 1490
- Park, J.-Y., & Woon, D. E. 2006, *ApJ*, 648, 1285
- Persson, M. V. 2014
- Pilling, S., Seperuelo Duarte, E., Domaracka, A., et al. 2010, *A&A*, 523, A77
- Pontoppidan, K. M., Dullemond, C. P., van Dishoeck, E. F., et al. 2005, *ApJ*, 622, 463
- Pontoppidan, K. M., Boogert, A. C. A., Fraser, H. J., et al. 2008, *ApJ*, 678, 1005
- Rocha, W. R. M., & Pilling, S. 2015, *ApJ*, 803, 18
- . 2018, *MNRAS*, 478, 5190
- Rocha, W. R. M., Pilling, S., de Barros, A. L. F., et al. 2017, *MNRAS*, 464, 754
- Rothard, H., Domaracka, A., Boduch, P., et al. 2017, *Journal of Physics B Atomic Molecular Physics*, 50, 062001
- Schutte, W. A., Tielens, A. G. G. M., Whittet, D. C. B., et al. 1996, *A&A*, 315, L333
- Shen, C. J., Greenberg, J. M., Schutte, W. A., & van Dishoeck, E. F. 2004, *A&A*, 415, 203
- Smith, R. L., Pontoppidan, K. M., Young, E. D., & Morris, M. R. 2015, *ApJ*, 813, 120
- Ulrich, R. K. 1976, *ApJ*, 210, 377
- van Dishoeck, E. F., Kristensen, L. E., Benz, A. O., et al. 2011, *PASP*, 123, 138
- Watanabe, N., Shiraki, T., & Kouchi, A. 2003, *ApJL*, 588, L121
- Whitney, B. A., Wood, K., Bjorkman, J. E., & Wolff, M. J. 2003, *The Astrophysical Journal*, 591, 1049
- Williams, J. P., & Cieza, L. A. 2011, *ARA&A*, 49, 67
- Zhang, Y., & Jin, L. 2015, *The Astrophysical Journal*, 802, 58

APPENDIX

A. DECONVOLUTION OF THE PROFILE BETWEEN 5.5–7.5 μm

The spectral region between 5.5–7.5 μm contains several O-H and C-H vibrational modes that might be associated to alcohols, ketone, and aliphatic ethers (Schutte et al. 1996; Gibb et al. 2000; Keane et al. 2001; Boogert et al. 2008, 2015). In order to determine the contribution of CH_3OH and HCOOH in the spectral profile between 5.5–7.5 μm , a Gaussian decomposition of this spectral range by using 5 components was employed as given by:

$$G(\lambda; A, \sigma) = \frac{A}{\sigma\sqrt{2\pi}} \exp\left[-\frac{(\lambda - \lambda_0)^2}{2\sigma^2}\right] \quad (\text{A1a})$$

$$\tau_\lambda = \sum_{i=0}^{m-1} G(\lambda^i; A^i, \sigma^i) \quad (\text{A1b})$$

where λ is the wavelength, A is the integrated area, and σ is the full width at half maximum of the Gaussian profile. Equation A1a is the Gaussian function of one component and Equation A1b is the sum of all components, assumed equal to 5 in this paper. Figures 11-16 show the Gaussian decomposition of the spectral range between 5.5–7.5 μm according to the evolutionary stage variation and ice processing level. The two components around 6.0 μm are associated with H_2O and daughter species formed from the ice processing. The blue shaded component at 6.8 μm is attributed to CH_3OH whereas the yellow shaded component at 7.24 μm refers to HCOOH . The component in between (~ 7.0 μm) has been attributed to CH_3CHO in Pilling et al. (2010).

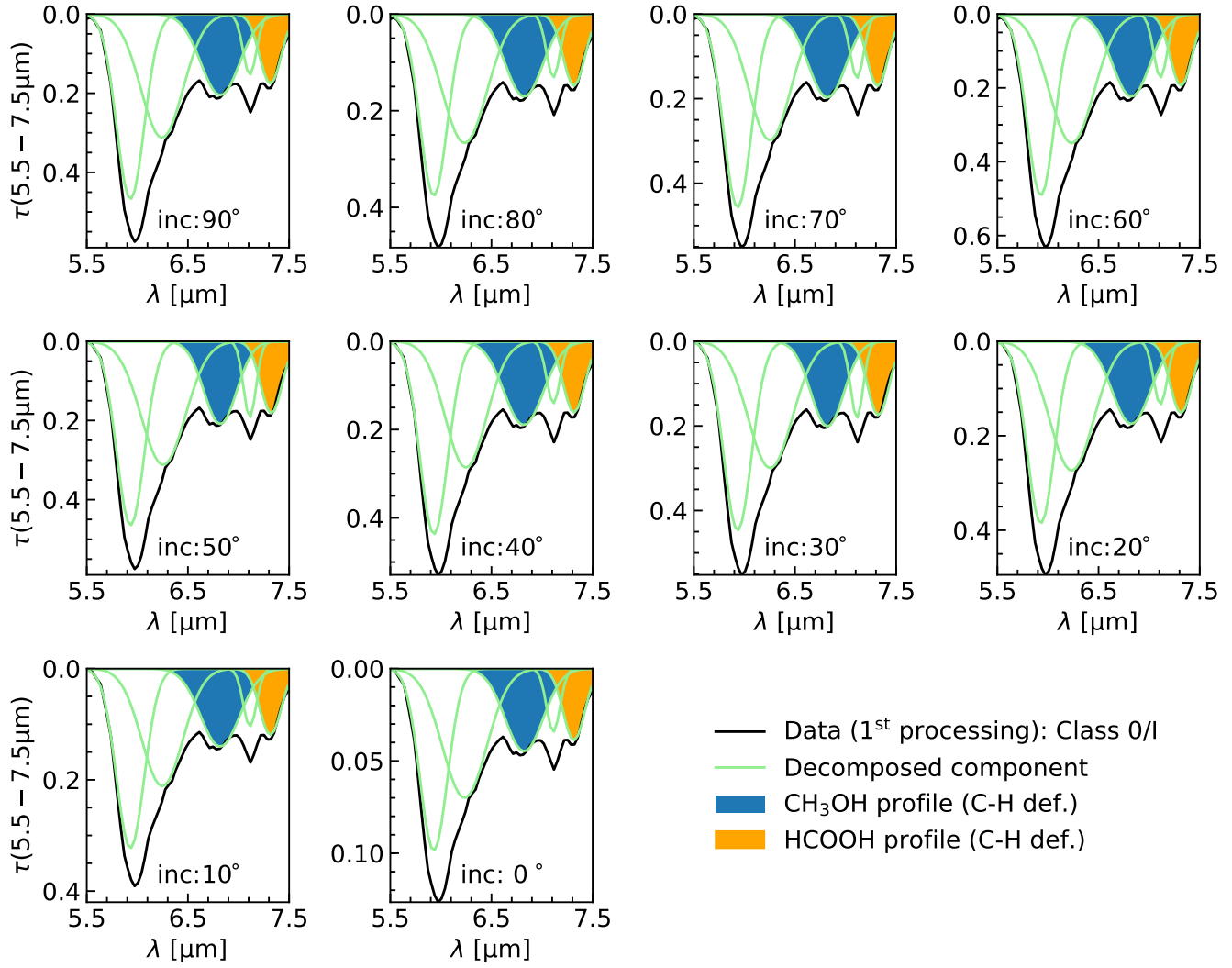


Figure 11. Decomposition of the optical depth between 5.5–7.5 μm for the 1st processing model and Class 0/I. The black line shows the modelled data, whereas the green lines indicated the Gaussian profiles. The contribution of CH_3OH and HCOOH are given by the blue and orange areas, respectively.

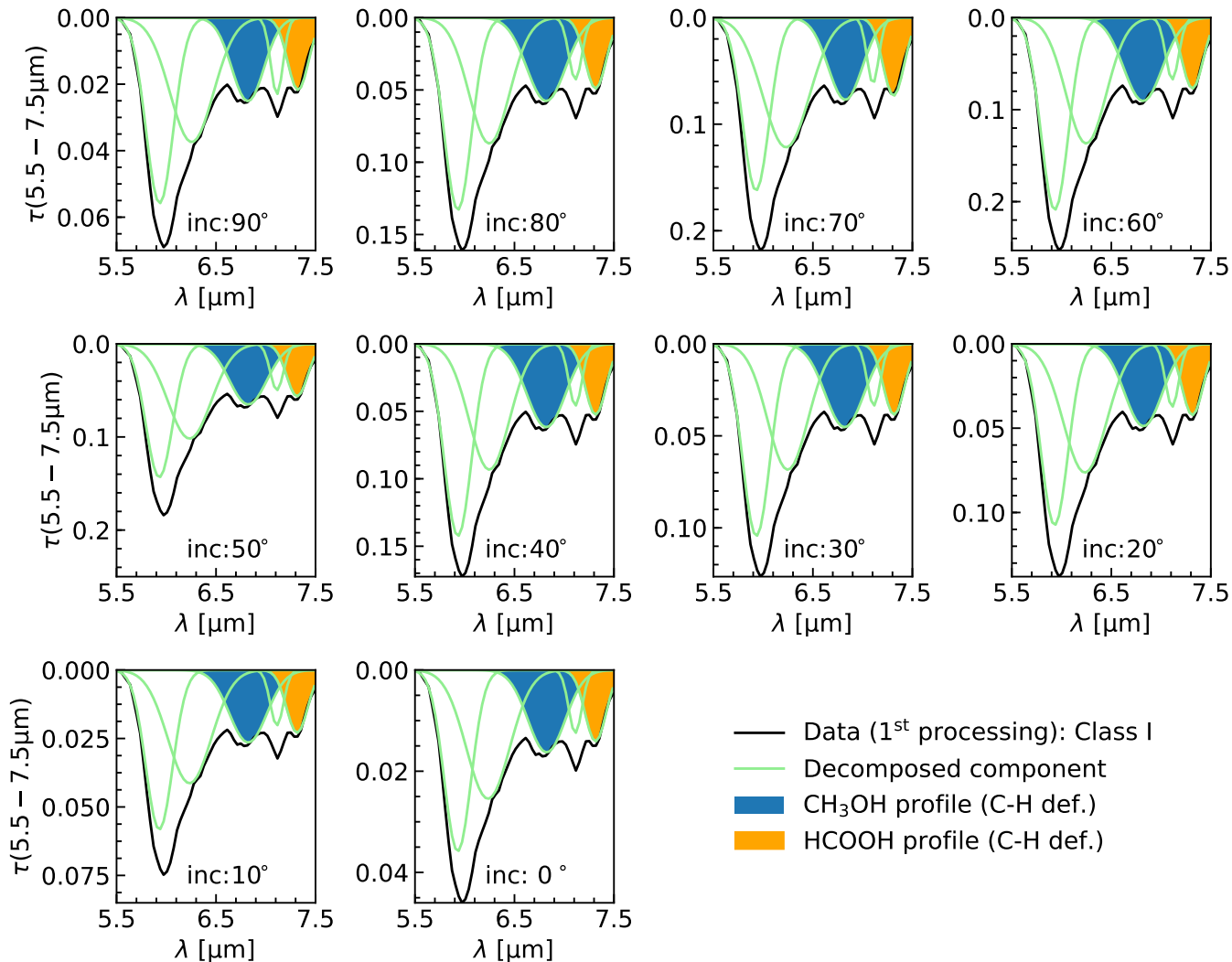


Figure 12. Same of Figure 11 for Class I.

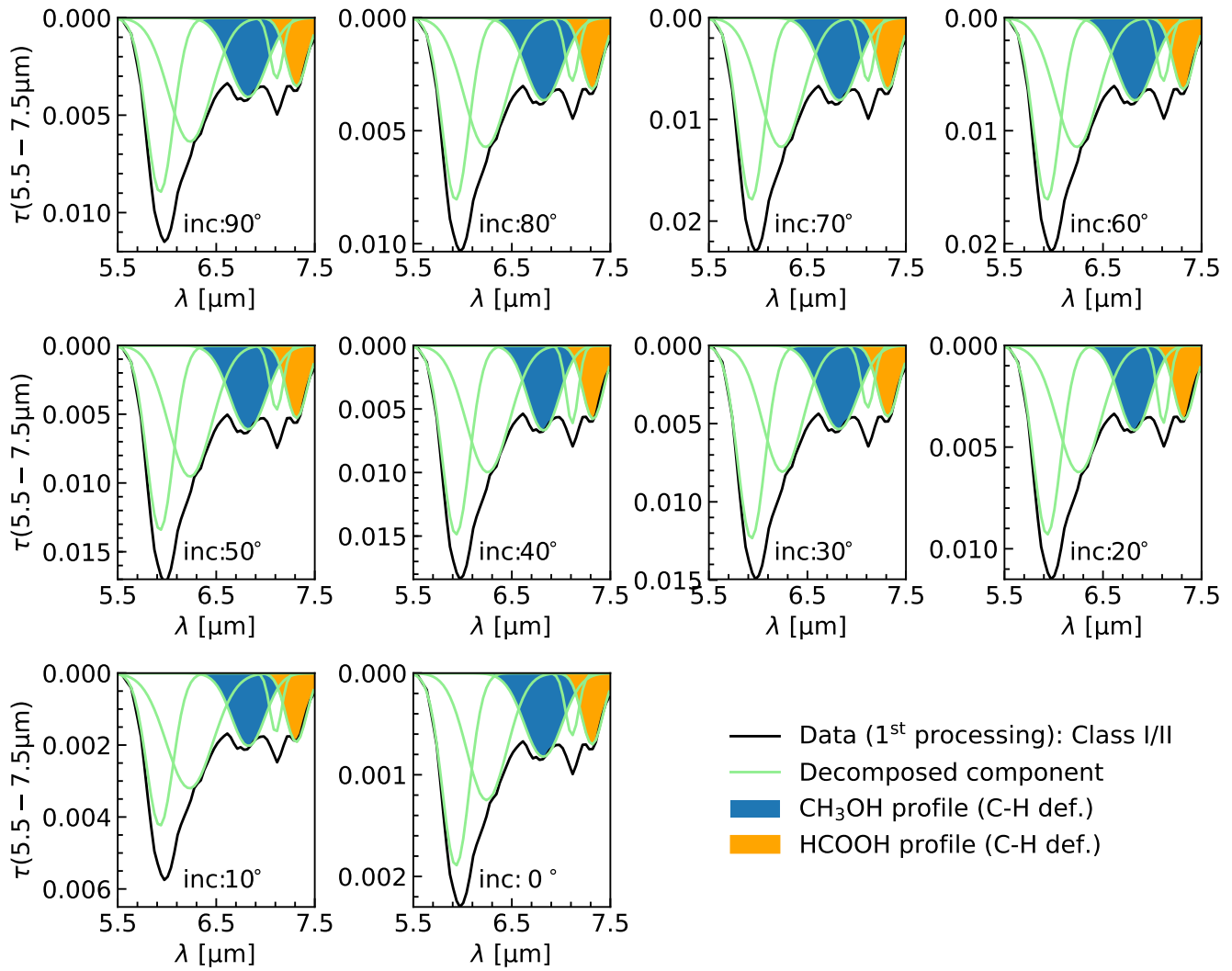


Figure 13. Same of Figure 11 for Class I/II.

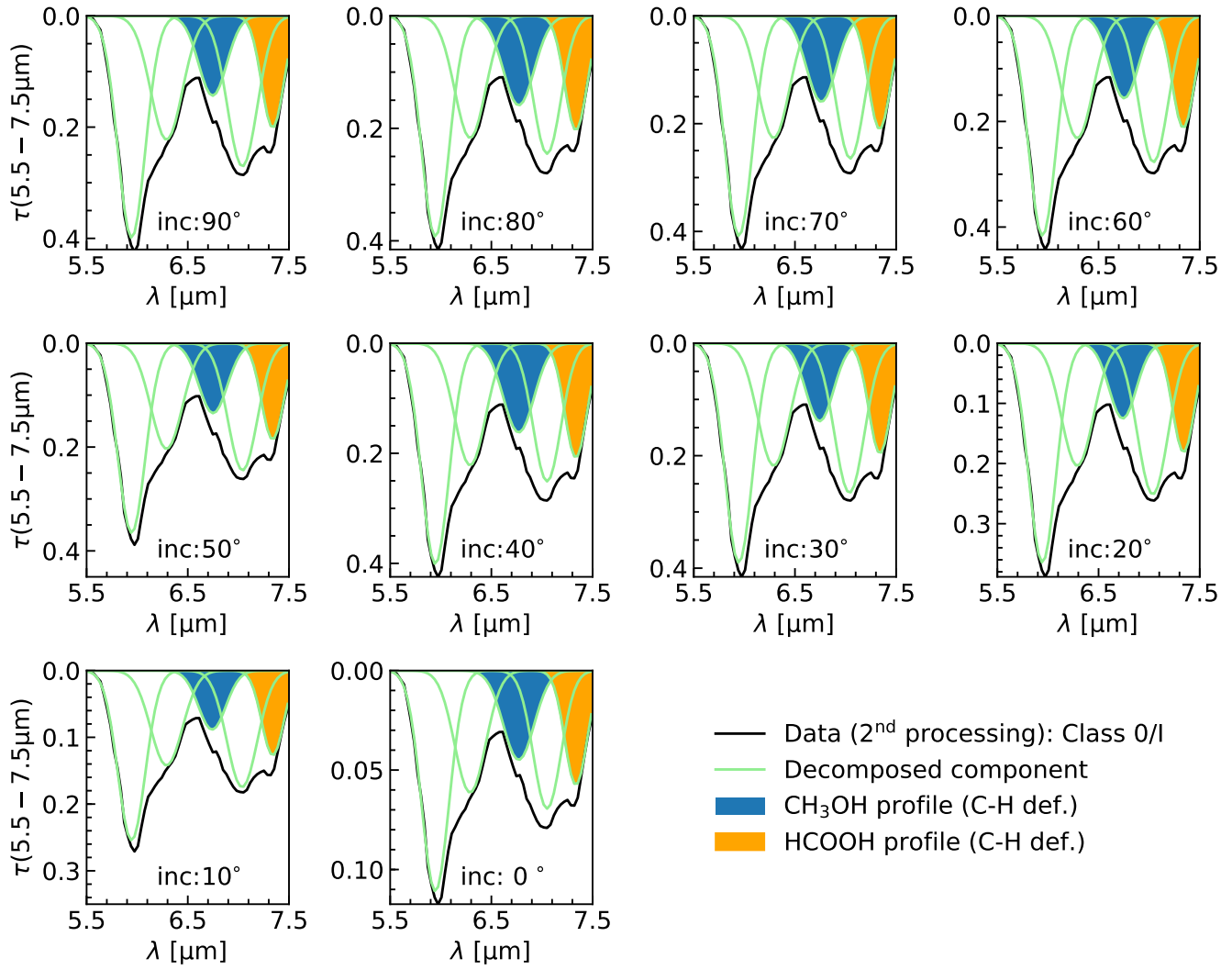


Figure 14. Same of Figure 11 for the 2nd processing model and Class 0/I.

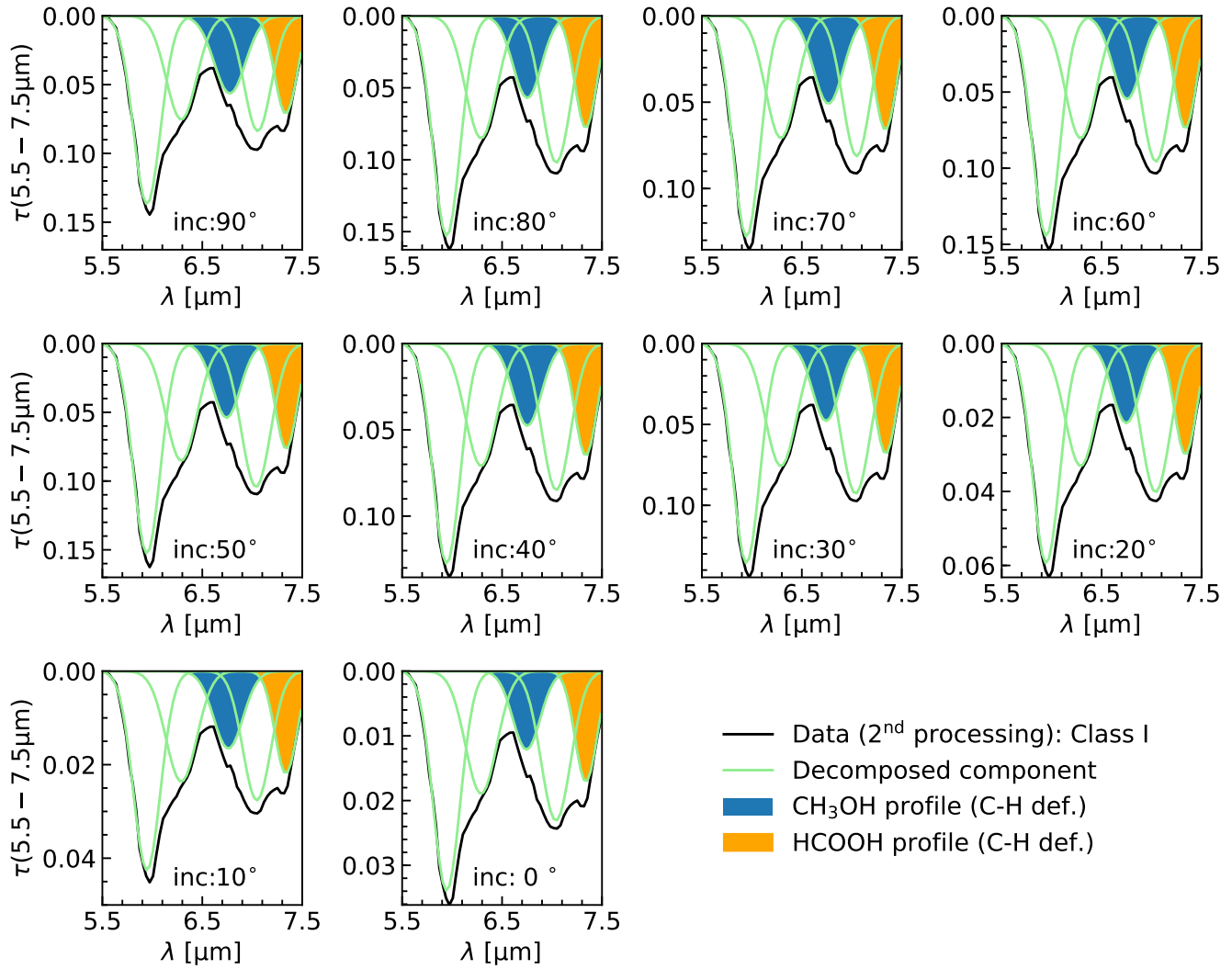


Figure 15. Same of Figure 11 for the 2nd processing model and Class I.

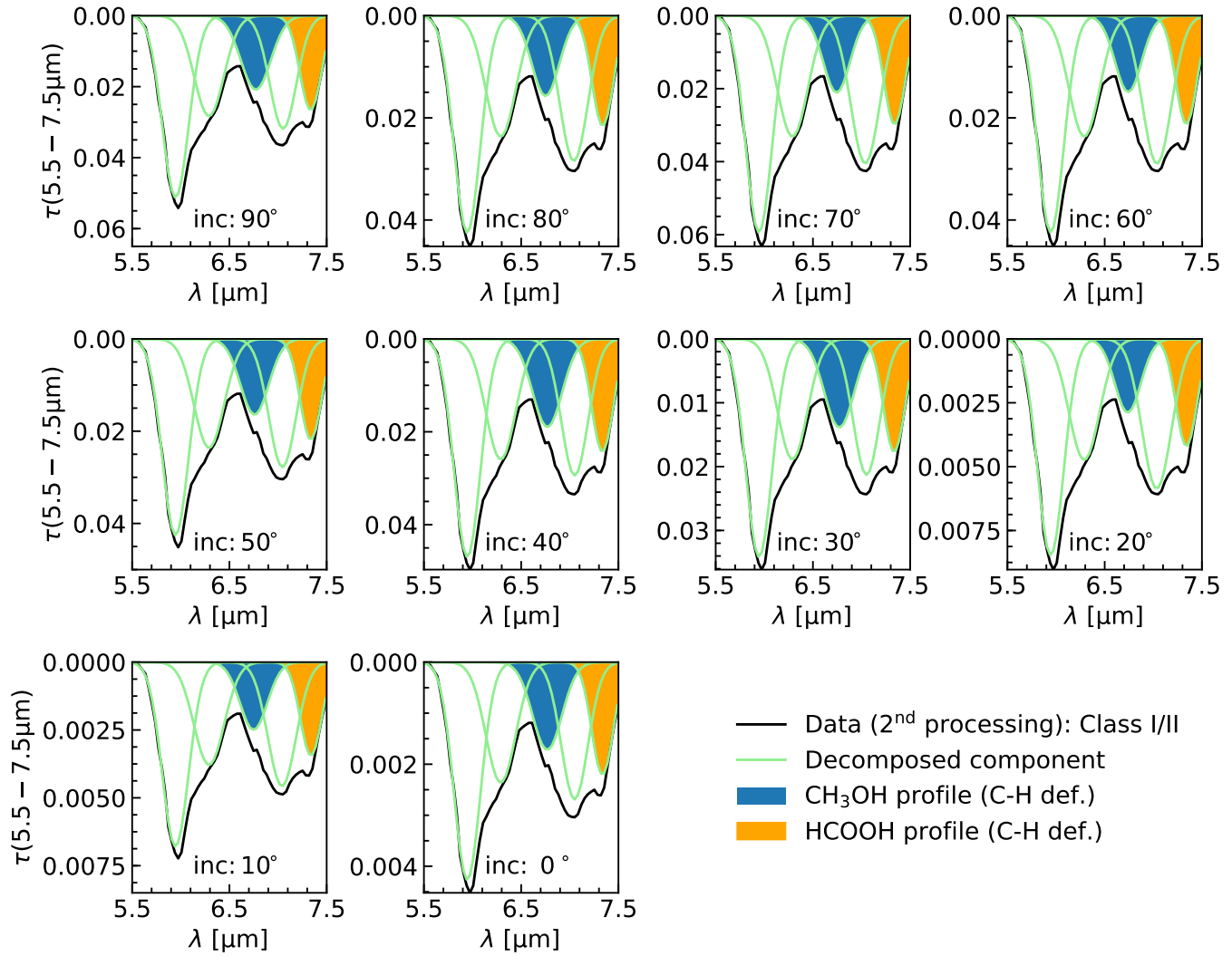


Figure 16. Same of Figure 11 for the 2nd processing model and Class I/II.